Electronic Supplementary Material (ESI) for Energy & Environmental Science.
This journal is © The Royal Society of Chemistry 2024

Supporting Information

Surface Charge-Reinforced and Ion-Selective Layers for Stable Metal Zinc Anodes Chemistry

Zhiquan Wei[a], Shixun Wang[a], Dedi Li[a], Shuo Yang[a], Songde Guo[c], Guangmeng Qu[d], Yihan Yang[d], Hongfei Li[*b]

[a] *Department of Materials Science and Engineering, City University of Hong Kong, Hong Kong, 999077, China.*

[b] *School of System Design and Intelligent Manufacturing, Southern University of Science and Technology, Shenzhen, 518055, China. Email: lihf@sustech.edu.cn*

[c] *Faculty of Materials Science and Energy Engineering/Institute of Technology for Carbon Neutrality, Shenzhen Institute of Advanced Technology, Chinese Academy of Sciences (CAS) Shenzhen, Guangdong, 518055, China.*

[d] *Songshan Lake Materials Laboratory, Dongguan, Guangdong, 523808, China.*

Table of contents

Page NO.

Methods

1. Materials

Zinc sulfate heptahydrate ($ZnSO_4 \cdot 7H_2O$, analytical reagent), Zinc trifluoromethanesulfonate ($Zn(OTF)_2$, analytical reagent), N-methyl-pyrrolidone (NMP, analytical reagent), ethanol (analytical reagent), Polytetrafluoroethylene preparation (PTFE, 60wt%) and Cysteamine (C_2H_7NS, 99.9%) were purchased from Aladdin. Graphite paper (10 μm, conductive collector), Polyvinylidene difluoride (PVDF-900, 99.5%) and Ketjen black ECP-600JD (KB, conductive agent) were purchased from CANRD. Ti mesh (99.9%, 100 mesh), stainless steel mesh (SS, 99.99%, 100 mesh), and Cu foil (99.8%, 20 μm) were obtained from Kangwei Metal. Zn foil (50 μm and 80 μm, 99.99%) was purchased from Chenshuo Metal. The active carbon powder (AC, YP-50F) with a particle size of 5-20 μm and a surface area of 1500-1800 $m^2\ g^{-1}$ was obtained from KURARAY.

2. Fabrication of I_2 cathode

low loading I_2 cathode: the AC was first coated on the graphite paper as hosting materials by mixing well with KB and PVDF in NMP solvent with weight ratios of AC : KB : PVDF of 8 : 1 : 1, while the loading mass of AC is 2 mg cm^{-2}. The I_2 electrode was soaked in the AC substrate (1.53 cm^2) in a solution of 1 M KI and 0.2 M $ZnSO_4$ for 12 h. After soaking, the AC collector was washed with DI water and then dried in the oven at 40 °C to serve as the cathode in Zn-I_2 coin cells, where the average areal capacity of active material was designated at 3 mg cm^{-2}.

High loading I_2 cathode: the AC was first coated on the Ti mesh as hosting materials by mixing well with KB and PTFE in ethanol solvent with weight ratios of AC : KB : PTFE of 8 : 1 : 1, while the loading mass of AC is 30 mg cm^{-2}. Then, the I_2 electrode was electrodeposited to the large-sized AC substrate (4 cm * 4 cm) in a solution of 1 M KI and 0.2 M $ZnSO_4$ under a constant current of 100 mA, where the average areal capacity of iodine was designated at 6 mAh cm^{-2}. After I_2 deposition, it was washed with DI water and then dried in the oven at 40 °C to serve as the cathode in Zn-I_2 pouch cells.

3. Electrochemical characterization

Symmetric cells (Zn||Zn), half cells (Zn||Cu and Zn||SS), and full cells were assembled using both bare Zn as anodes in CR-2032 coin cells, while a volume of 100 μL of electrolyte (2 M $ZnSO_4$ in bare Zn based system; 2 M $ZnSO_4$ with 1 mM cysteamine in Zn@SCRIS-SAL based system) was utilized with the glass fiber (Waterman-1820) as the separator. The galvanostatic charging-discharging processes

based on different current densities from 0.5 to 20 mA cm^{-2} was conducted using the CT2001A or CT3002A Battery Cycler (Wuhan, China). Cyclic voltammetry, Tafel plot, and Chronoamperograms were measured using a CHI-760 electrochemical working station. All SCRIS-SALs-based cells are resting for 0.5 h to form the self-assembled layers and then proceed with electrochemical characterizations.

4. Characterizations

Adhesion and friction measurements were made with a Digital Instruments (Santa Barbara, CA) Nanoscope III multimode scanning force microscope equipped with a fluid cell. Zeta potential (ξ) measurements were performed by dynamic light scattering analysis (zeta sizer Nano ZS-90). The crystal structure was studied by X-ray diffraction (XRD, X'Pert Pro MPD, Philips, Holland) using Cu Kα as the radiation source under 40 kV and 40 mA. Morphologies were probed by scanning electron microscopy ((SEM, FEI Quanta 450 FEG SEM) equipped with energy-dispersive spectroscopy (EDS). X-ray photoelectron spectroscopy (XPS) spectra were recorded on a photoelectron spectrometer (ESCALAB 250, Thermo Scientific, America), where the binding energy (BE) of the elements was calibrated by the BE of C 1s (284.80 eV). The modulus mapping was measured by atomic force microscope (Bruker, DIMENSION ICON) and conducted in the quantitative nano-mechanics mode (QNM). Raman measurement (Dxr-2xi, Thermo Scientific, America) was performed with in situ homemade cells to observe the O-H stretching peak. The air pressure test is based on a sealed chamber home-designed, and a barometer is used to detect the change in air pressure during symmetric cell cycling.

5. Density functional theory (DFT) calculation

Electrostatic potential (ESP) mappings were carried out with the Gaussian 09W software package to gain structural information of the abovementioned molecules. Geometrical optimization adopted the B3LYP method with 6-31+G(d,p) basis sets. Based on the optimized structure of molecules, ESP analysis on van der Waals surface was done to deduce the possible SCRIS-SAL functional sites using the Multiwfn 3.3.8 software package in the Gaussian 09W software package.[1]

The structures of Zn^{2+} or $H^+ \cdot H_2O$, Zn@SCRIS-SALs with the non-protonation or whole protonation and bare Zn, and their complex (Zn@SCRIS-SALs or bare Zn with Zn^{2+} or $H^+ \cdot H_2O$) were first optimized by using the density functional theory (DFT) at the B3LYP/def2-TZVP level.[2] All

geometry optimizations, including the implicit solvent model with SMD were performed using the DFT-D3 method in ORCA.[3, 4] Then, the single-point energies of complexes were done at the same level after the previous optimization, which considering basis set superposition error (BSSE). The harmonic frequency calculations were carried out at the same level of theory to help verify that all structures have no imaginary frequency. The binding energy of the configuration (E_{bind}) was calculated by the following equation:

$$E_{bind} = E_{AB} - (E_A + E_B)$$

where E_A, E_B, and E_{AB} respectively represent the energies of A (Zn^{2+}) and B (single SCRS-SALs) and the complex energy, a negative value of E_{bind} indicates that the process is an exothermic reaction and a high negative value corresponds to a stronger interaction, which indicates more heat release and a more stable product.

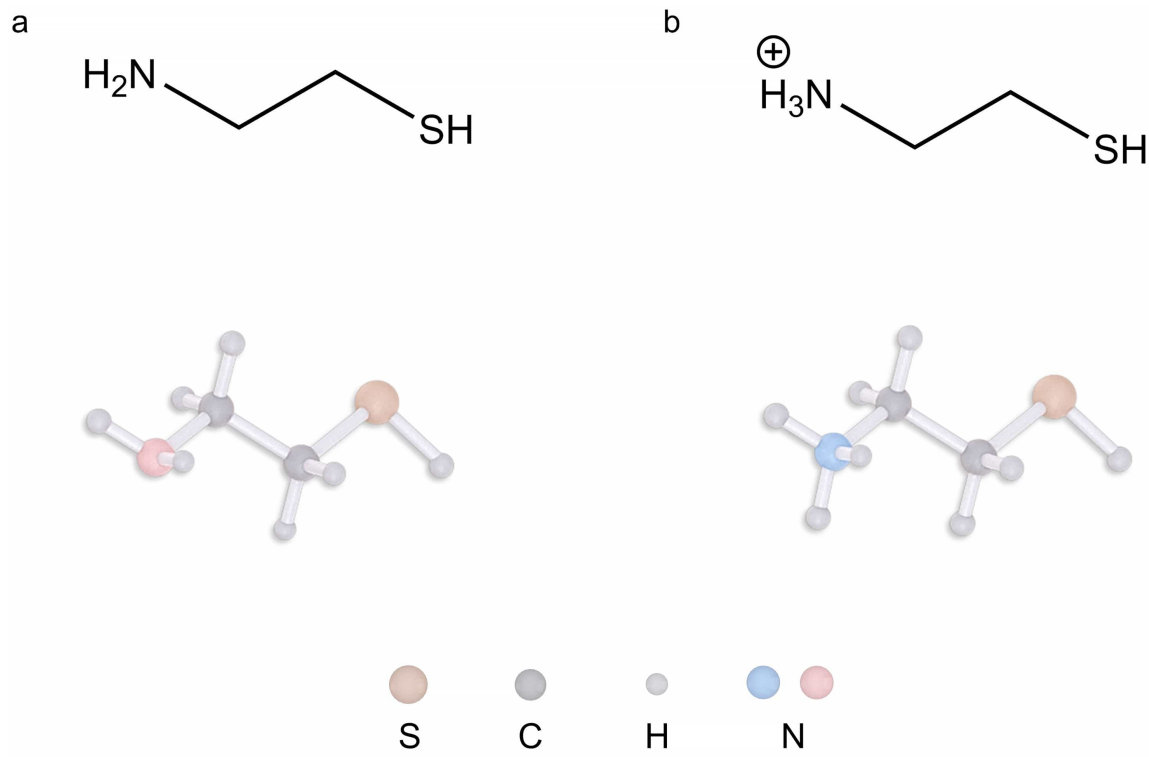

Fig. S1 The molecular structure of cysteamine with the (a) non-protonation and (b) whole protonation state.

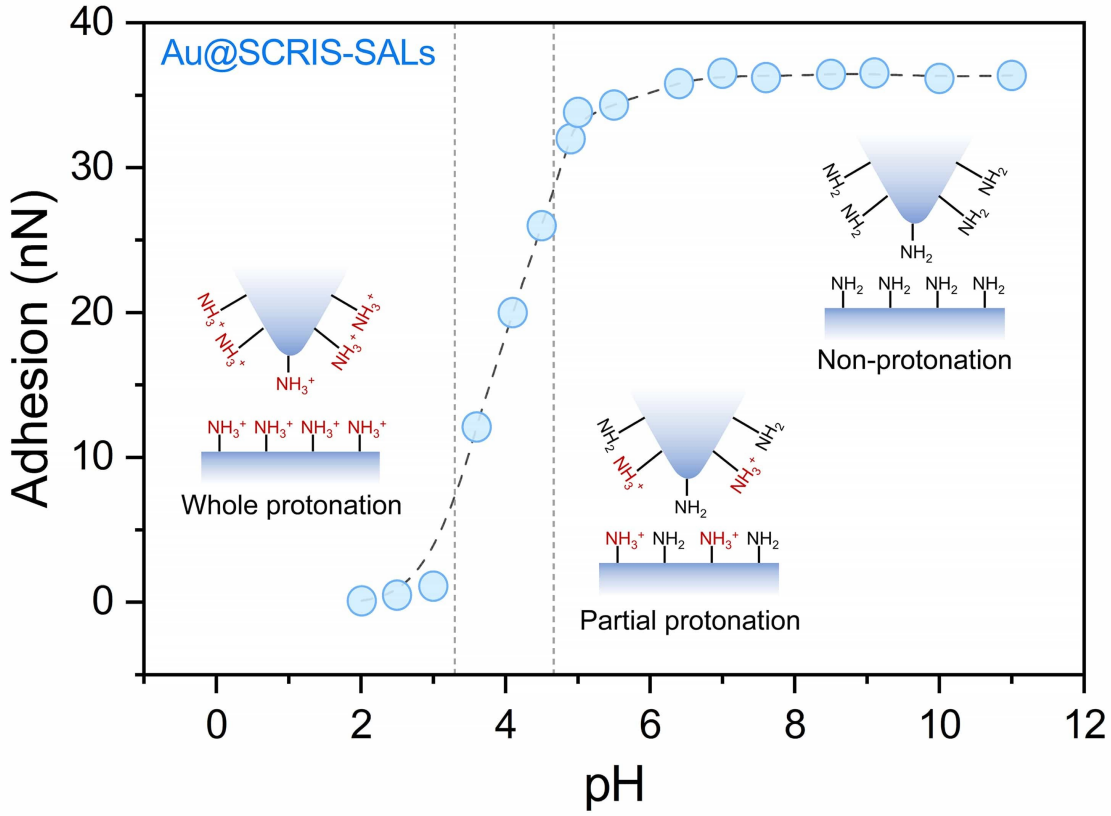

Fig. S2 Adhesion force between the Au nanoparticles and tip functionalized with cysteamine SALs terminating with amine groups under different pH conditions, wherein adhesion force represents a mean value obtained from more than 100 single measurements.

Note: According to the previous works and **Fig. S2**,[5, 6] average adhesion force values obtained at different solution pH values (100 individual force measurements for each pH value) for tips and Zn functionalized with cysteamine SALs terminating with amine groups (Tips@SCRIS-SAL & Au@SCRIS-SALs) are plotted to show the interfacial chemistry of the surface functionality. The results show that the adhesion force drops sharply to zero (indicating a repulsive interaction) below a pH of 4. The decrease and elimination of an attractive force between the tip and sample are consistent with the protonation of the amine groups on these two surfaces. SALs with terminal functional groups $-NH_2$ were found to be highly sensitive to the changes in the ionization state of the terminal functionalities induced by varying the solution pH, showing that the whole protonation ($-NH_3^+$) is in pH$\leq$ 3, partial protonation ($-NH_3^+$ & $-NH_2$) is in pH of approximately 3 to 5, and non-protonation ($-NH_2$) is in pH$\geq$ 5.

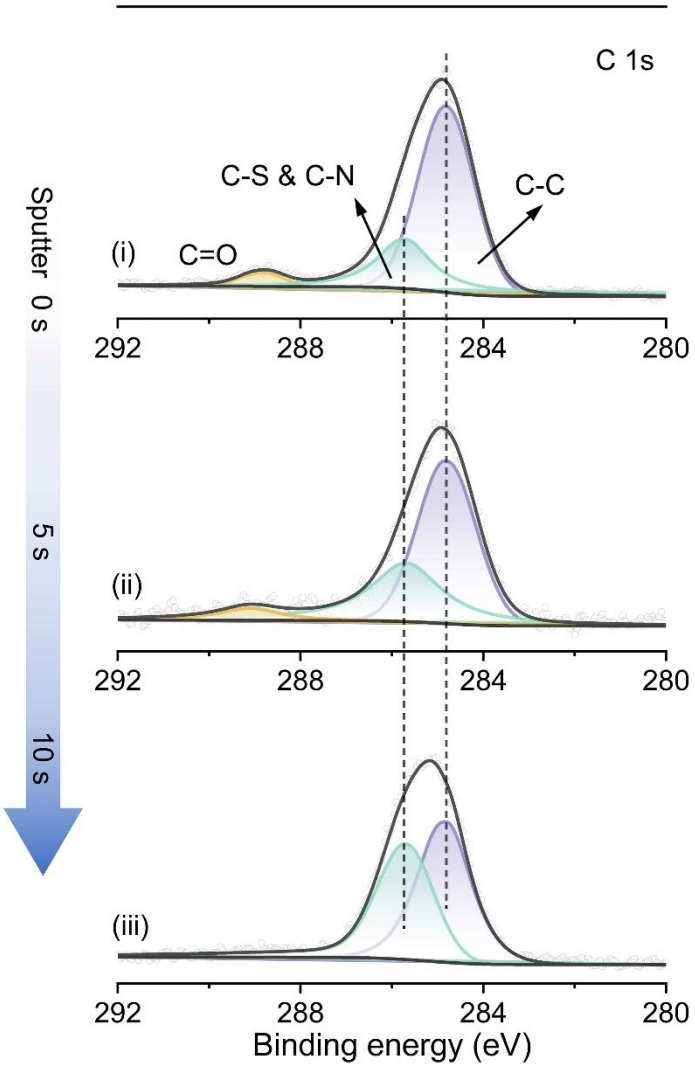

Fig. S3 Depth etching profiles from high-resolution C 1s spectrum of Zn@SCRIS-SALs anodes.

Note: As reflected by the high-resolution C 1s spectrum of Zn@SCRIS-SALs (**Fig. S 3**), the slight peaks situated at 285.8 eV before etching correspond to C-S & C-N species.[7] Then, the obvious peaks of C-S & C-N showed after etching, implying the SCRIS-SALs is located at the bottom of the Zn anode surface layer.

.

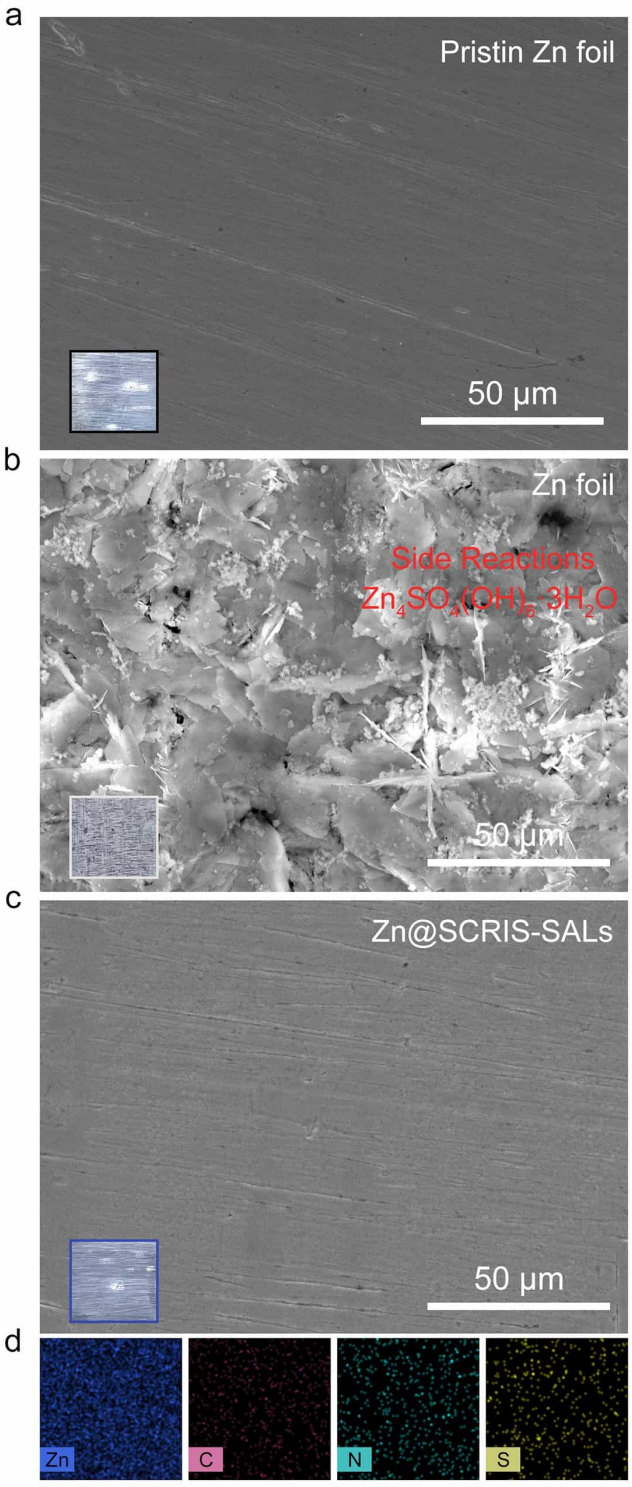

Fig. S4 SEM images of (a) bare Zn and bare Zn after soaking in (b) 2 M $ZnSO_4$ and in (c) 2 M $ZnSO_4$ with 1 mM cysteamine (Zn@SCRIS-SALs) for 12 h corresponding to (d) elemental mapping. The inset corresponds to photographs.

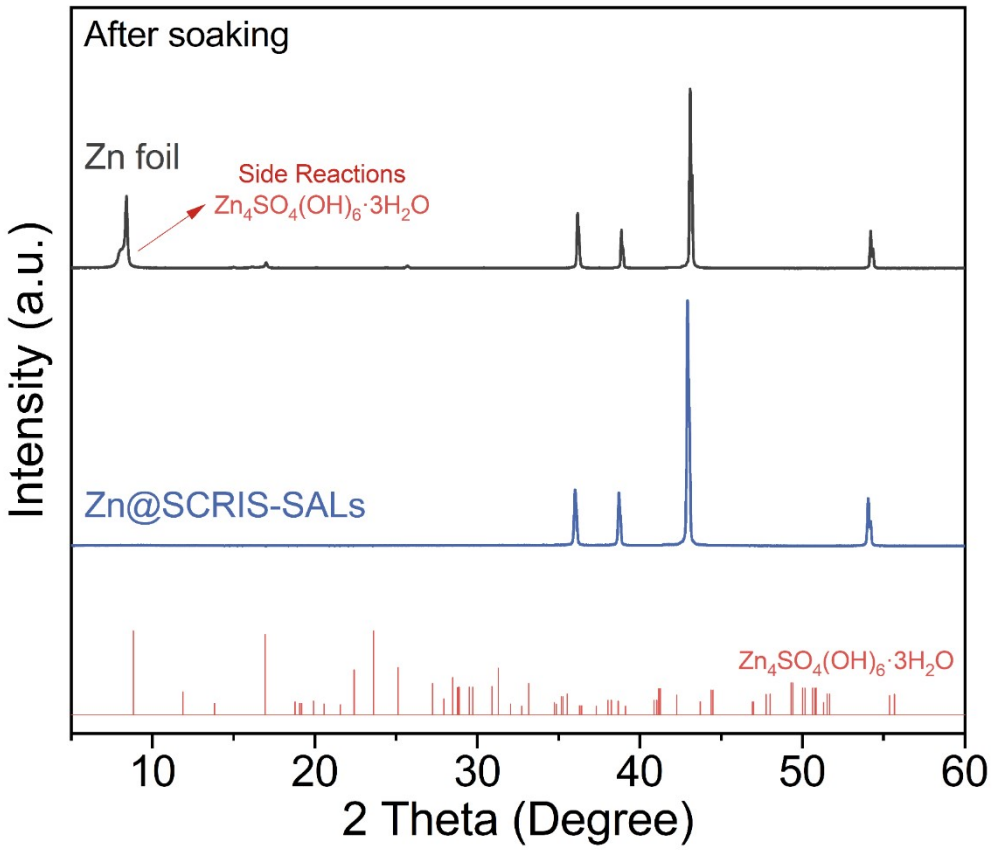

Fig. S5 XRD pattern of bare Zn after soaking in 2 M $ZnSO_4$, bare Zn after soaking in 2 M $ZnSO_4$ with 1 mM cysteamine (Zn@SCRIS-SALs) for 12 h and by-products of $Zn_4SO_4(OH)_6{\cdot}4H_2O$ with PDF card.[8]

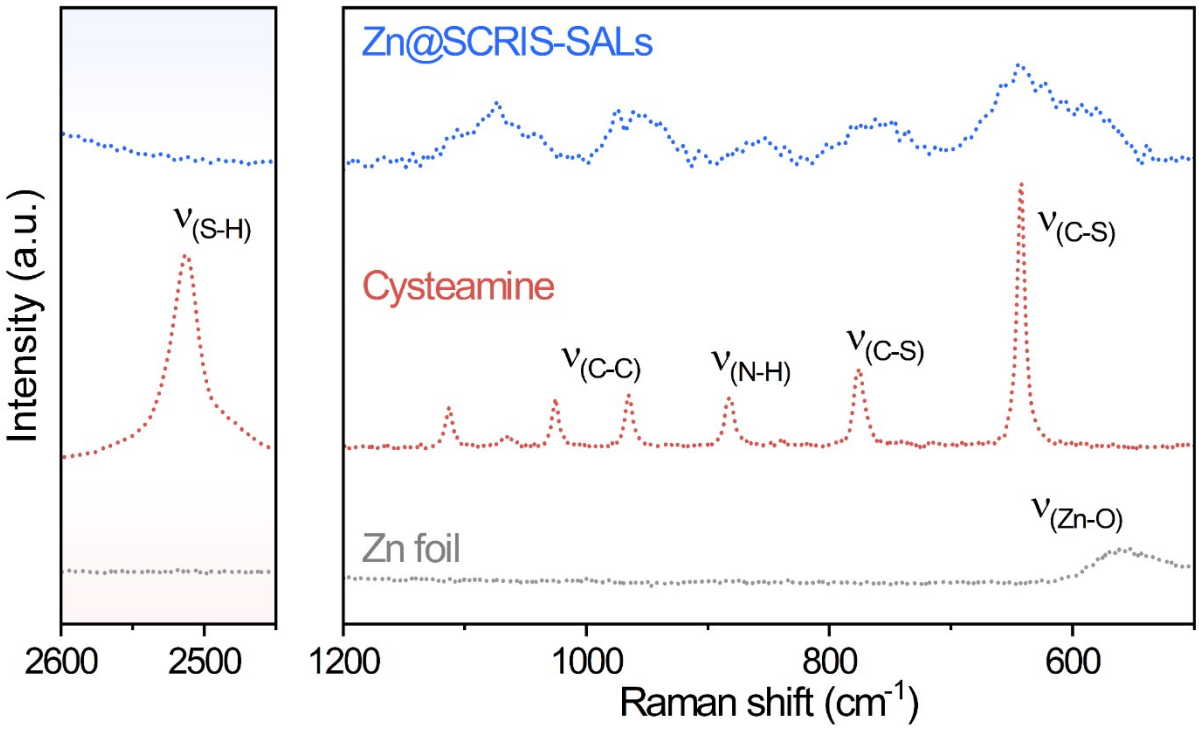

Fig. S6 Raman spectra of bare Zn after soaking in 2 M $ZnSO_4$ with 1 mM cysteamine (Zn@SCRIS-SALs) for 12 h, bare Zn and pure cysteamine.

Note: As shown in **Fig. S6**, the peaks at 645.4, 868.3, 960.6, and 975.1 cm^{-1} in Raman results of the Zn@SCRIS-SALs anode corresponded to the stretching and asymmetric vibration mode of C-C, N-H and C-S species, which is consistent with blank cysteamine. Interestingly, the bending assigned to the S-H stretching modes at 2548 and 2576 cm^{-1} disappeared on Zn@SCRIS-SALs indicating the chemical adsorption to form Zn-S covalent bonds.

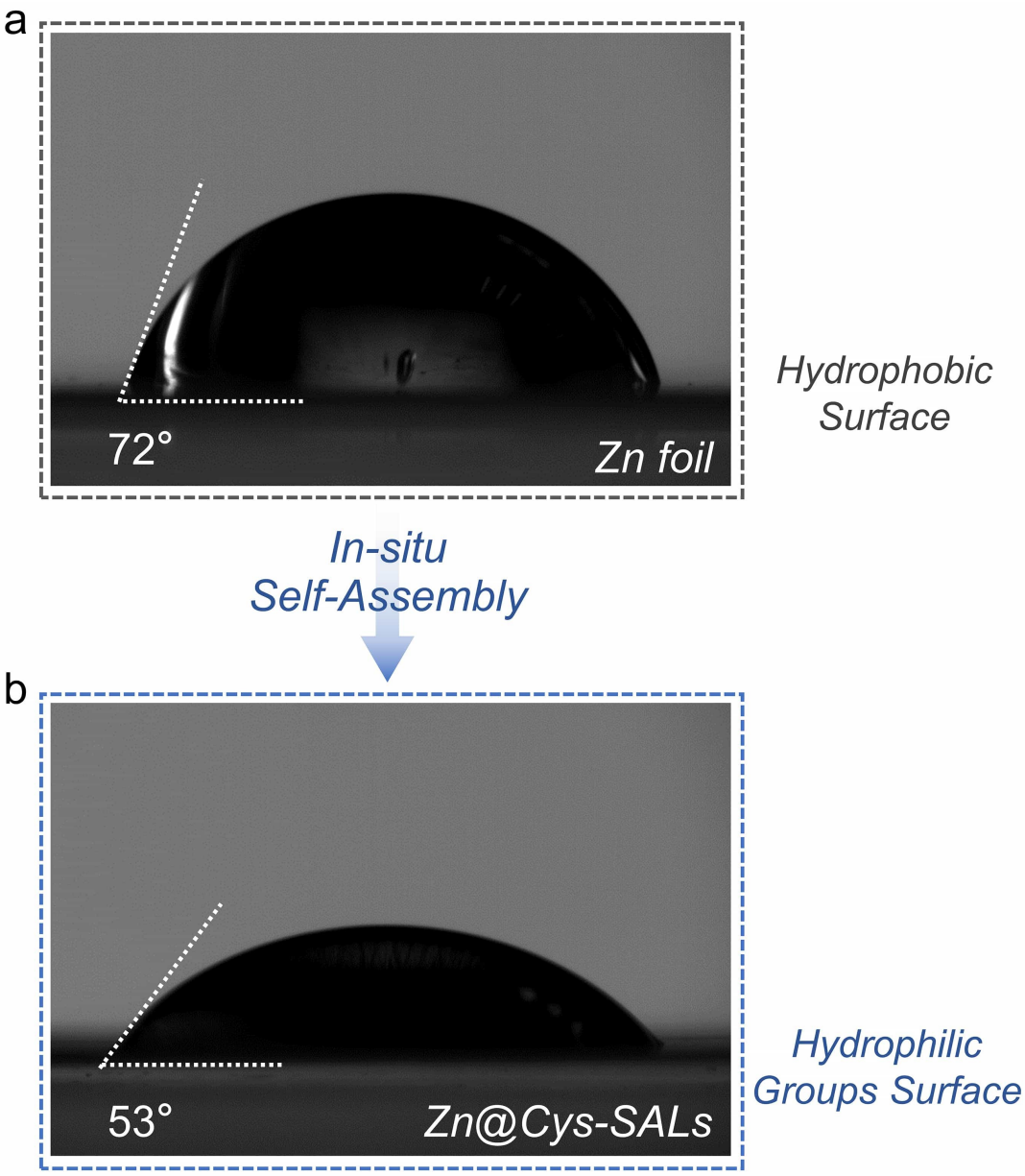

Fig. S7 Contact angles of (a) bare Zn and (b) Zn@SCRIS-SALs.

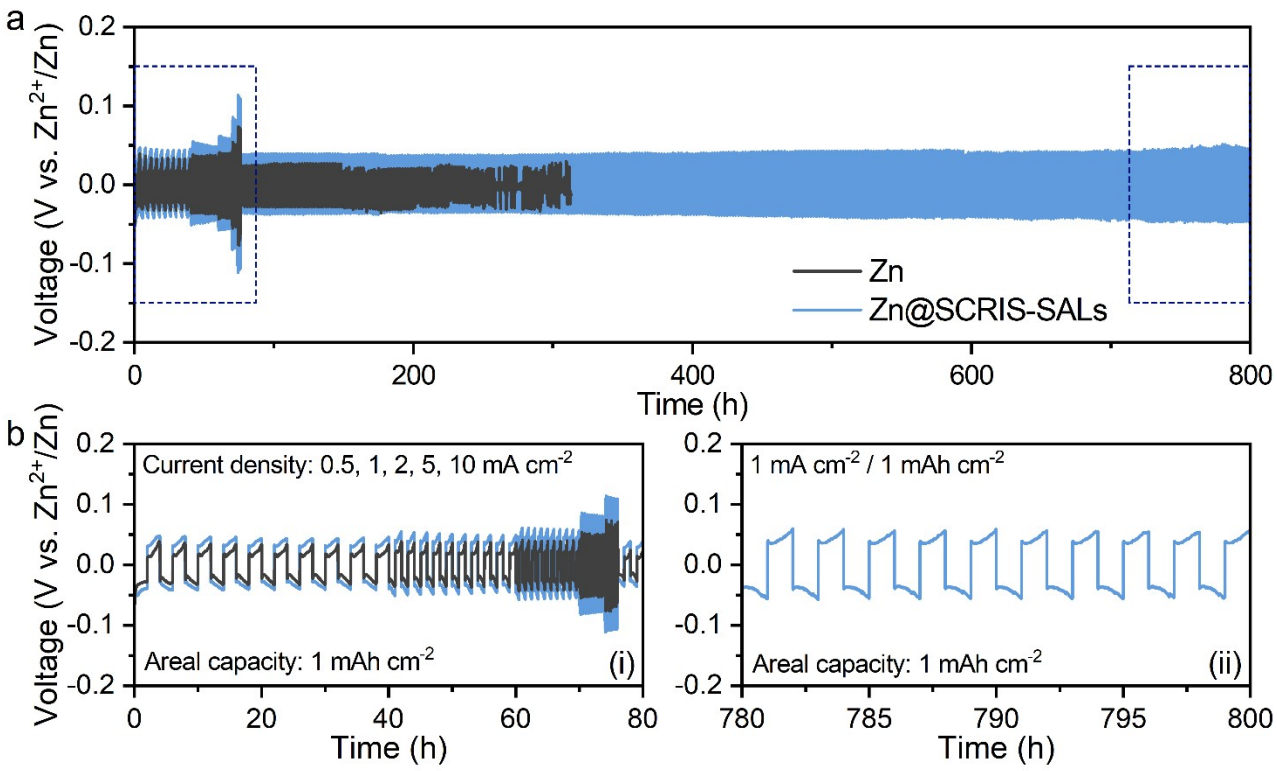

Fig. S8 Rate performances of the bare Zn and Zn@SCRIS-SALs and (b) the selected cycles corresponding to the region (i) (0-80 h) and region (ii) (780-800 h) in rate performances.

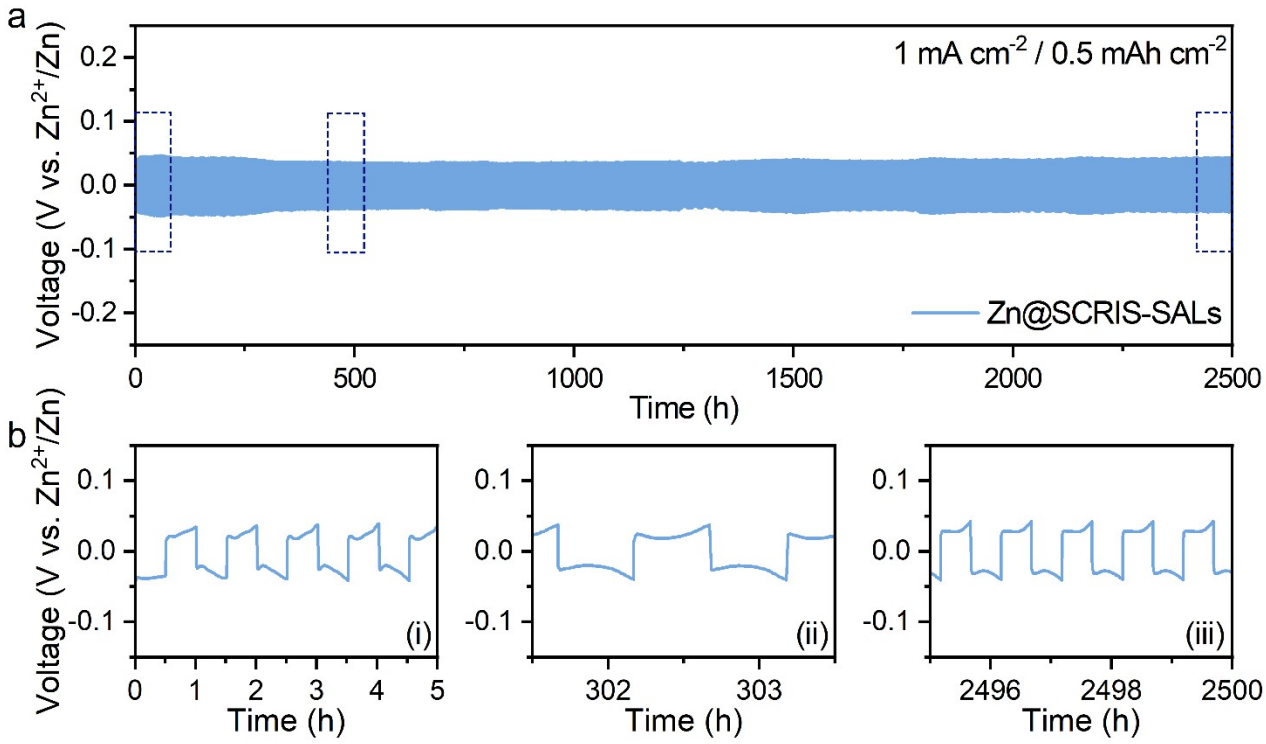

Fig. S9 Voltage-time curves of Zn@SCRIS-SALs symmetric cells with a capacity of 0.5 mA h cm^{-2} at 1 mA cm^{-2} and (b) the selected cycles corresponding to the region (i) (0–10 h) and region (ii) (1770-1780 h) in cycling performances.

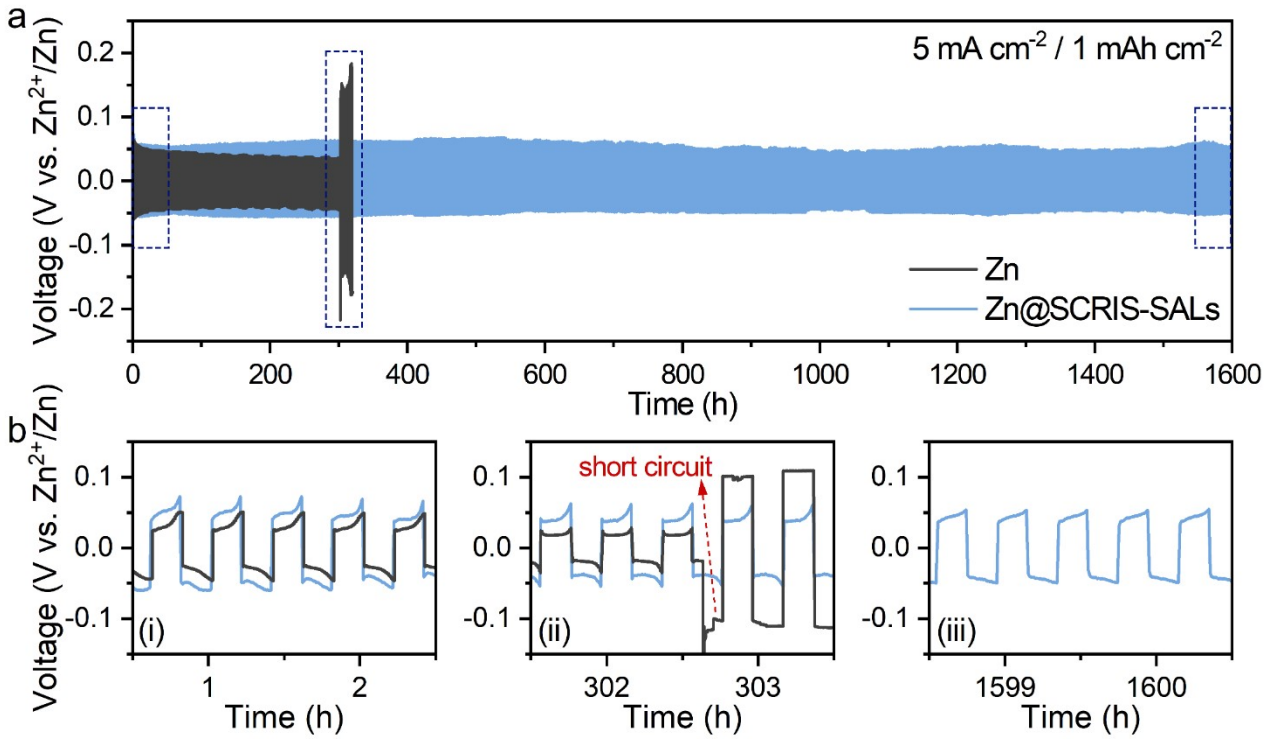

Fig. S10 Voltage-time curves of bare Zn and Zn@SCRIS-SALs symmetric cells with a capacity of 1 mA h cm^{-2} at 5 mA cm^{-2} and (b) the selected cycles corresponding to the region (i) (0-2 h), region (ii) (302-303 h) and region (iii) (1599-1600 h) in cycling performances.

Fig. S11 The photograph of (a) bare Zn and (b) Zn@SCRIS-SALs symmetric cells under a high areal capacity of 20 mAh cm^{-2} at a high current density of 10 mA cm^{-2} after 5 cycles.

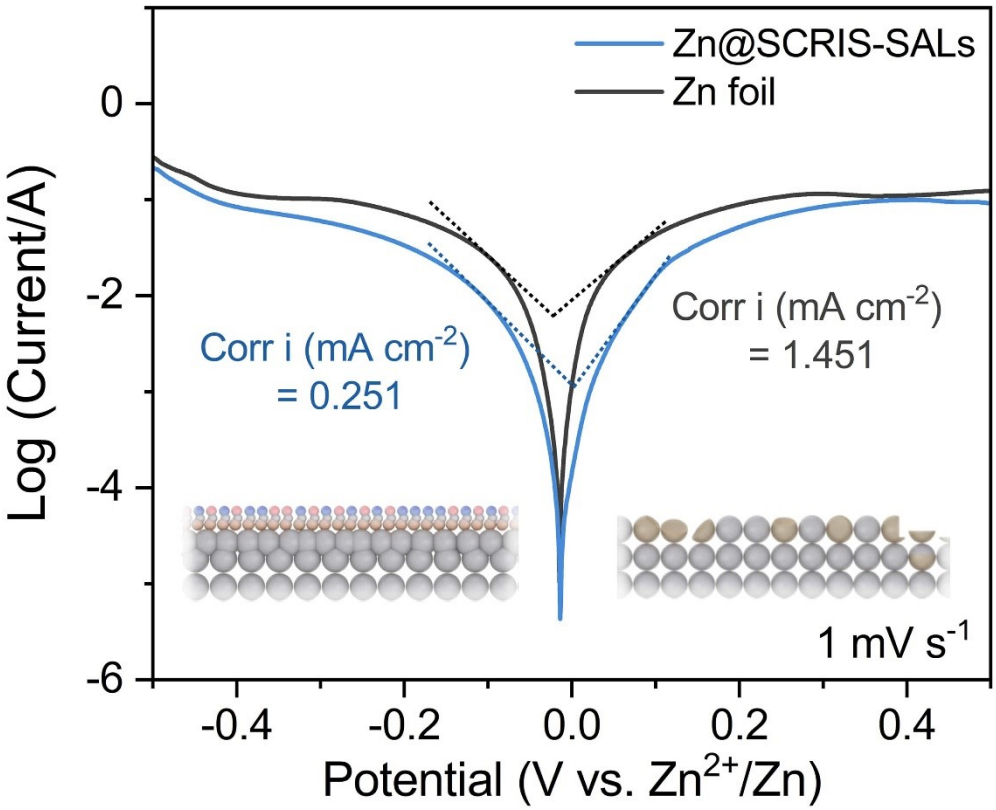

Fig. S12 Tafel plots of bare Zn and Zn@SCRIS-SALs symmetric cells at the scanning rate of 10 mV s^{-1}, marking the exchange current densities.

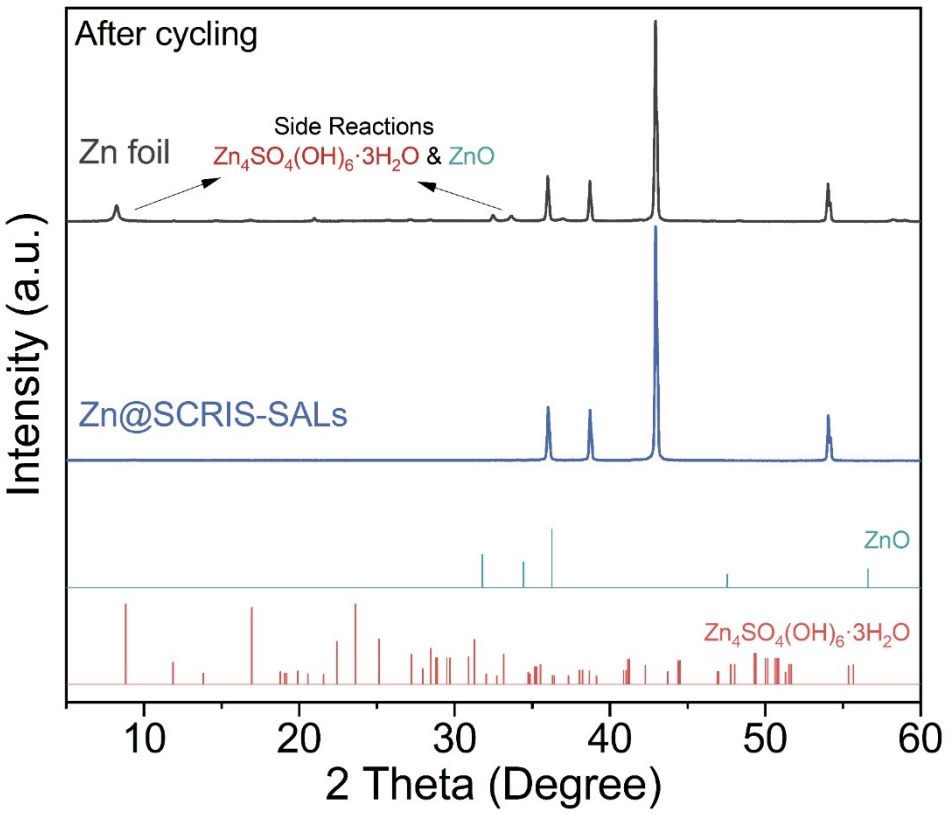

Fig. S13 XRD pattern of bare Zn, Zn@SCRIS-SALs anodes after 100 h with an areal capacity of 1 mA h cm^{-2} at 5 mA cm^{-2}, and by-products of ZnO (PDF#36-1451) & $Zn_4SO_4(OH)_6{\cdot}4H_2O$ (PDF#39-0689).[8, 9]

Note: After the cycling, peaks of by-products ZnO and $Zn_4SO_4(OH)_6{\cdot}4H_2O$ can be clearly observed in the cycled bare Zn anode. These by-products are typically associated with HER occurred at the unstable Zn surface during the Zn deposition process. The water molecules can compete with the Zn^{2+} to capture the electrons, generating H_2 and then leading to the increase of local pH value.[10]

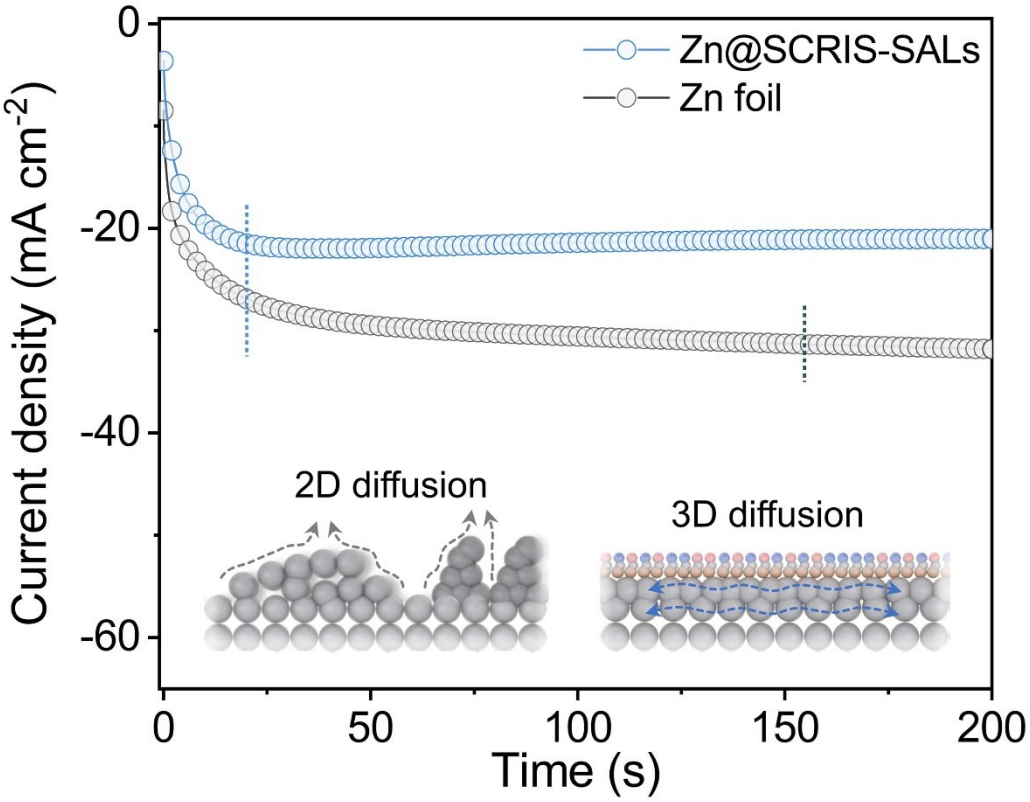

Fig. S14 Chronoamperograms (CA) of bare Zn and Zn@SCRIS-SALs symmetric cells at -150 mV overpotential.

Note: The variation in current versus time at a constant potential can sensitively reflect the nucleation process and surface change.[11] Schematics of the Zn^{2+} diffusion and reduction processes on bare Zn and Zn@SCRIS-SALs anodes, showing the Zn@SCRIS-SALs anode with 3D diffusion can be smooth in Zn deposition.

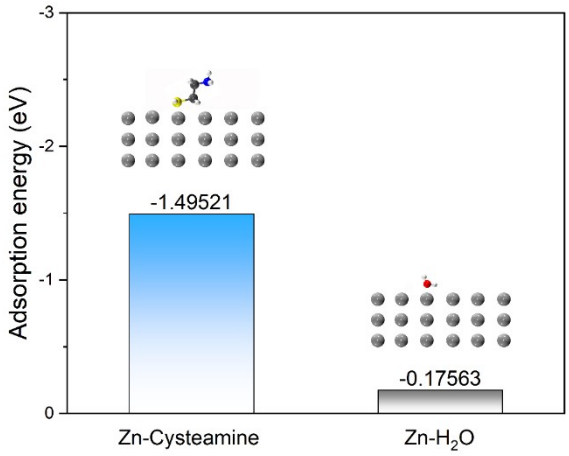

Fig. S15 Adsorption energy of cysteamine-Zn and H_2O-Zn metal surface.

Note: Density functional theory (DFT) calculations showed that cysteamine additives exhibited stronger adsorption energy than H_2O (**Fig. S15**), indicating that even stripped cysteamine would be able to preferentially adsorb on the surface of the Zn anode to dynamic patch on the Zn metal surface. This result can be attributed to the strongly conjugative capability of the thiol (-SH) functional group with metals.

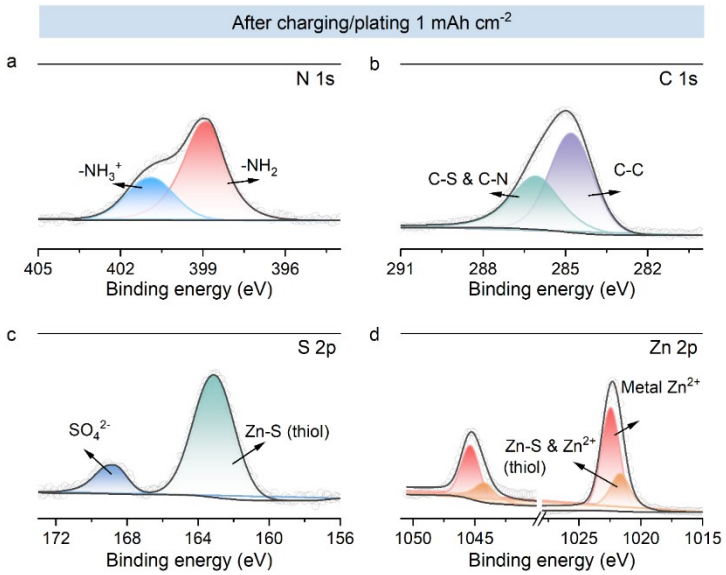

Fig. S16 (a) - (d) XPS analysis of the elements N, C, S, and Zn in the Zn@SCRIS-SAL after charging/plating 1 mAh cm^{-2} under sputtering 10 s with 1000 eV.

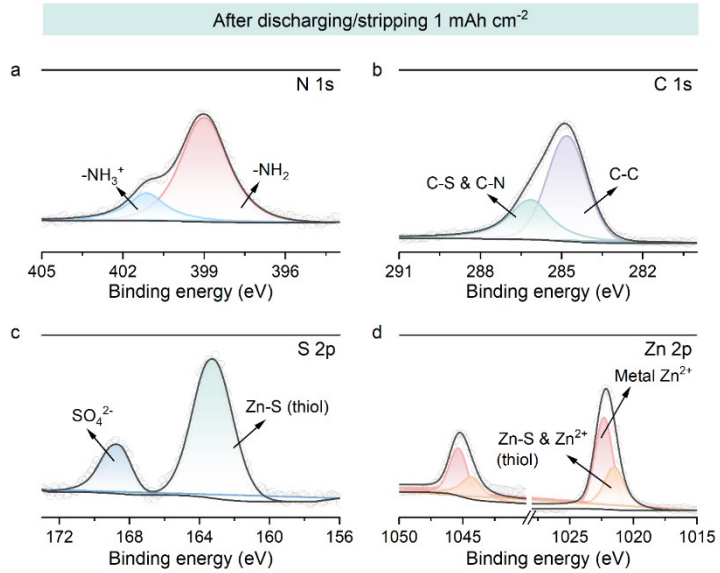

Fig. S17 (a) - (d) XPS analysis of the elements N, C, S, and Zn in the Zn@SCRIS-SAL after discharging/stripping 1 mAh cm^{-2} discharging under sputtering 10 s with 1000 eV.

Note: *ex-situ* XPS characterizations were further conducted to investigate the distribution of the SCRIS-SALs layer on the Zn metal-electrolyte interface after charging/plating and discharging/stripping. As displayed in **Fig. S17 and Fig. S18**, it can be observed the XPS result after Zn plating and stripping that the Zn anode surface showed obvious signals of $-NH_2/NH_3^+$ functional groups and Zn-S covalent bonds. The results demonstrated that cysteamine additives could conduct a dynamic replenishment ability in response to the change in electrode morphology. Notably, the similar XPS signals can also indicate the chemical stability of SCRIS-SALs layer, which would not be forming SEI.

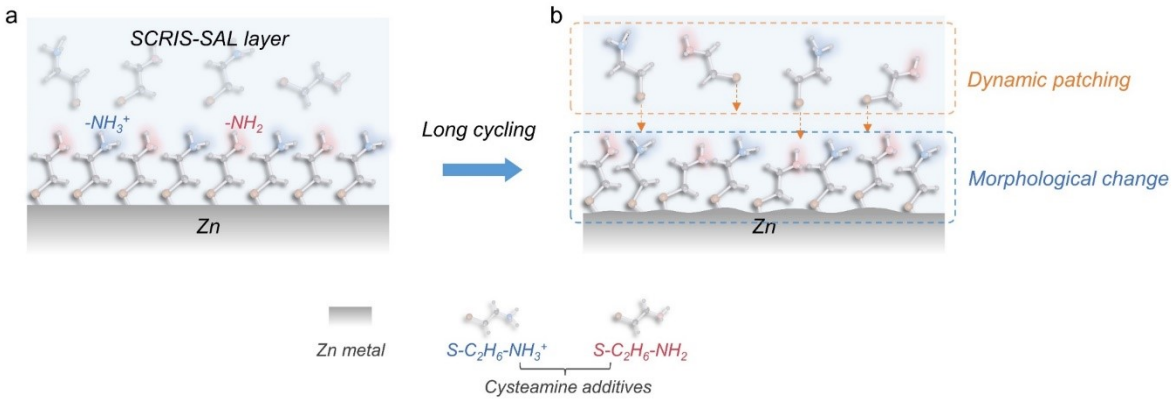

Fig.S18 Schematics of (a) SCRIS-SALs layer and (b) function at the Zn metal-electrolyte interface.

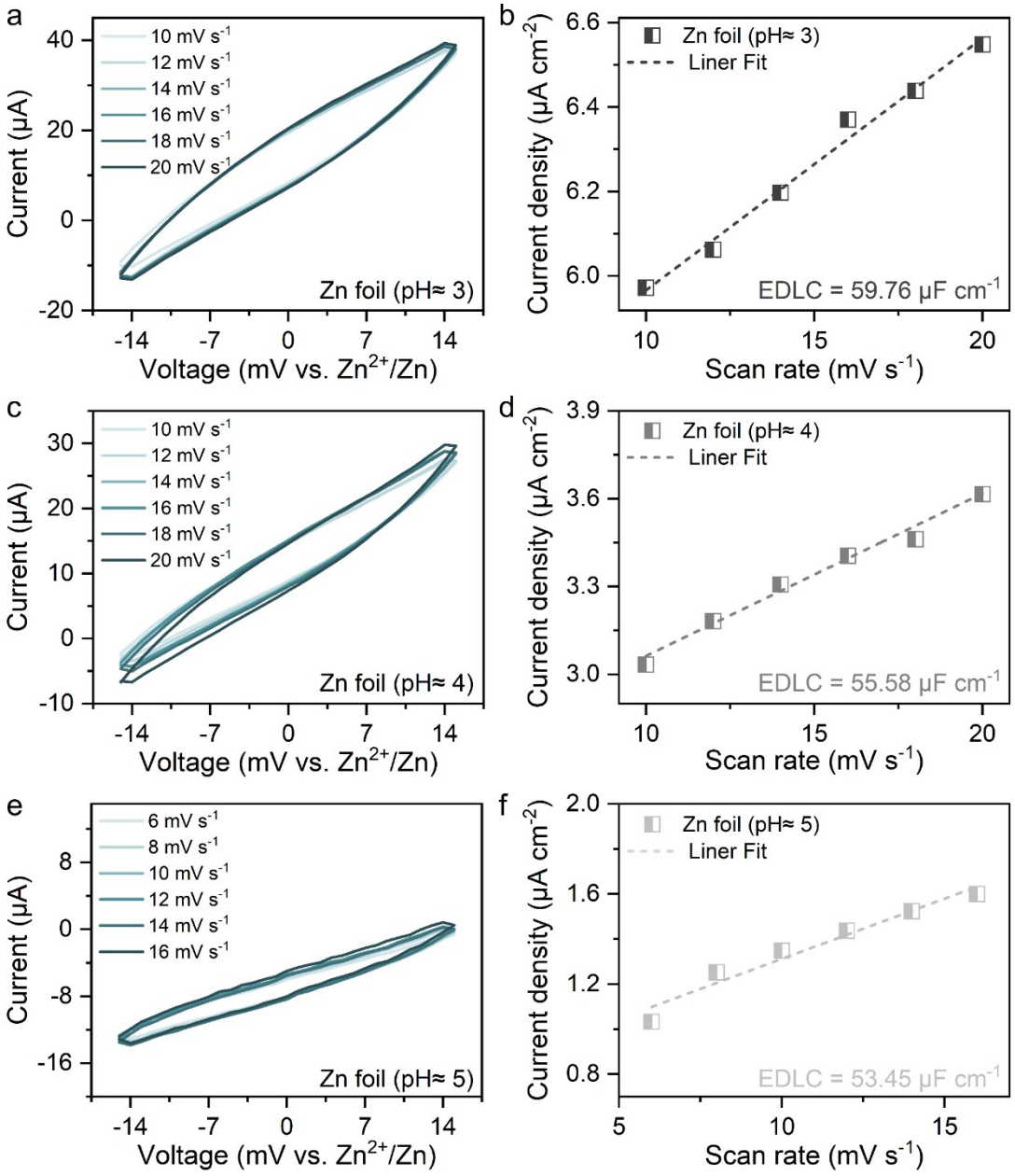

Fig. S19 Electric double layer capacitance measurements for the bare Zn anode in 2 M $ZnSO_4$ electrolytes under different pH conditions (pH = 3, 4, 5). (a, c & e) Cyclic voltammograms curves for Zn-Zn symmetric coin cells with different pH conditions (pH = 3, 4, 5) in a voltage range from -15 mV to 15 mV under various scanning rates, corresponding to (b, d & f) plots of capacitive currents versus scan rate.

Note: According to the previous report, the EDLC value was calculated by the equation as the follow:[12]

$$C = \frac{i}{v}$$

where C means the capacitance, i corresponds to the current and was defined by half of the difference between positive and negative scanning current at each scanning rate.

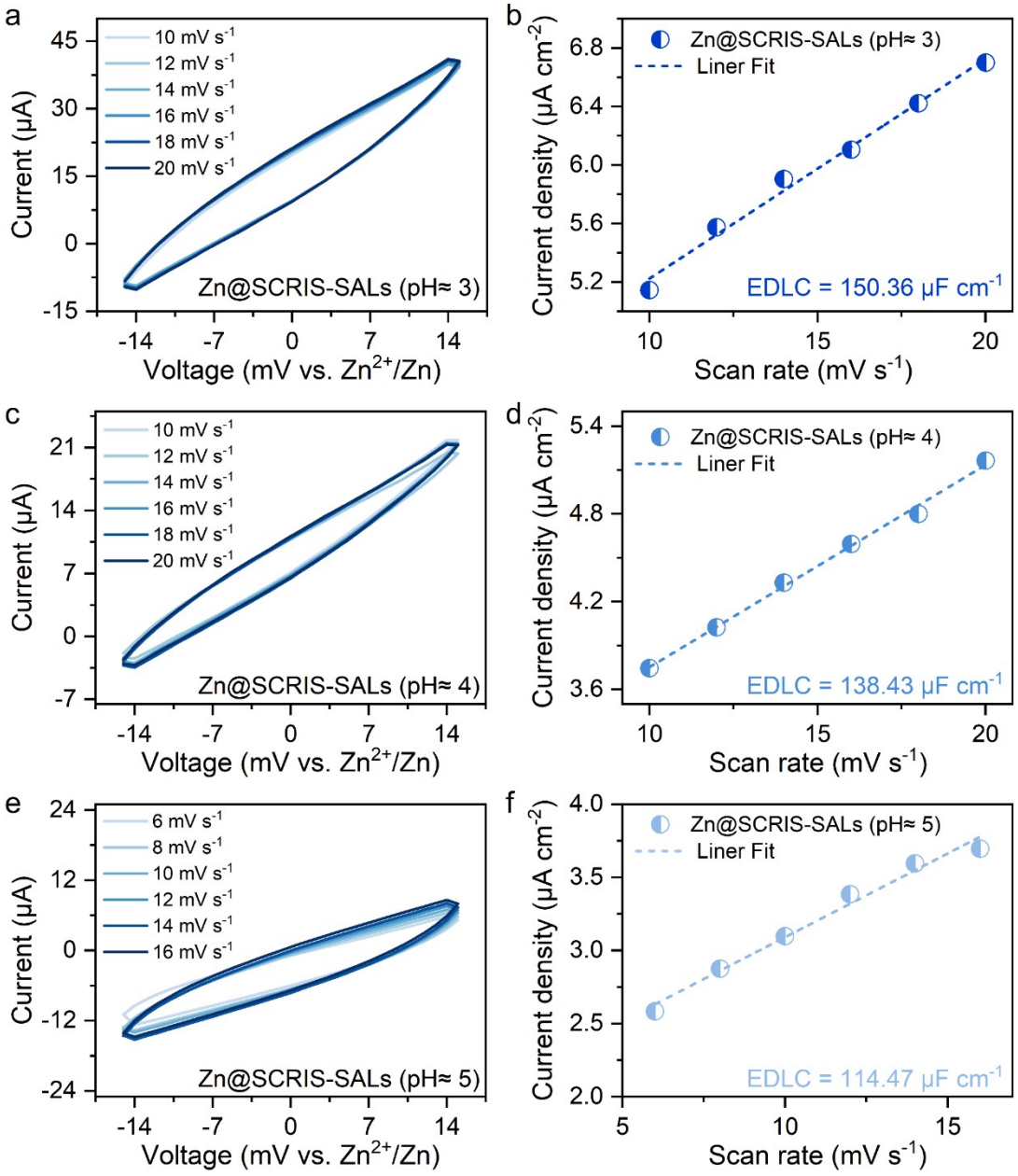

Fig. S20 Electric double layer capacitance measurements for the Zn@SCRIS-SALs anode in 2 M $ZnSO_4$ electrolytes with 1mM cysteamine under different pH conditions (pH = 3, 4, 5). (a, c & e) Cyclic voltammograms curves for Zn-Zn symmetric coin cells with different pH conditions (pH = 3, 4, 5) in a voltage range from -15 mV to 15 mV under various scanning rates, corresponding to (b, d & f) plots of capacitive currents versus scan rate.

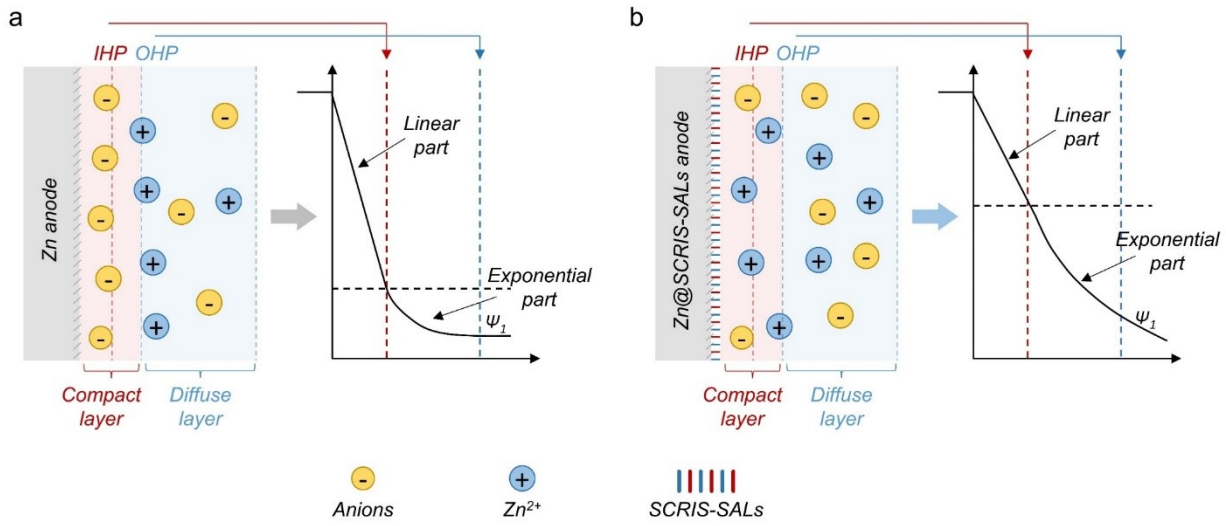

Fig. S21 Schematic of the EDL structure of (a) bare Zn and (b) Zn@SCRIS-SALs.

Note: The electrical double layer (EDL) structure is widely recognized as the crucial factor influencing the plating/stripping of Zn at the anode-electrolyte interface. As shown in **Fig. 5b**, Zn@SCRIS-SALs (138.43 μF cm^{-2}) displayed the highest capacity compared to bare Zn (55.58 μF cm^{-2}), indicating a structural alteration in the EDL on the electrode. According to the Gouy-Chapman-Stern model, the EDL at the interface comprises a compact layer and a diffusion layer. Notably, the electron transfer of Zn^{2+} occurs in the compact layer. The concentration of Zn^{2+} and the potential of the compact layer indirectly impact the activation energy of the electrode reaction.

According to the equation of equilibrium potential, the schematic of the EDL structure was displayed in **Fig. S21**. It can be observed that the bare Zn surface adsorbs more anions, leading to lower Zn^{2+} concentration in the compact layer (**Fig. S21a**). Conversely, SCRIS-SALs isolate the zinc metal surface from the electrolyte, thereby reducing direct anion adsorption. Meanwhile, abundant zincophilic sites facilitated the adsorption of many Zn^{2+} in the compact layer (**Fig. S21b**). The results indicated that the introduction of SCRIS-SALs would increase the potential difference in the compact layer, which can be attributed to repelling the anions and attracting Zn^{2+}, enabling the construction of high-concentration Zn^{2+}

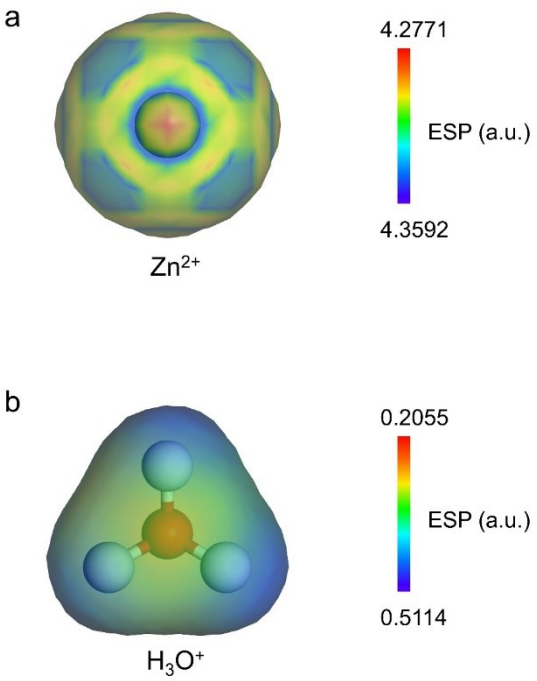

Fig. S22 ESP-mapping of ions with (a) Zn^{2+} and (b) H_3O^+. Surface local minima of ESP are represented as red spheres, and the corresponding ESP values are marked out by numbers.

Note: the electrostatic states were calculated to investigate the interaction of different ions and molecules (NH_3^+-CH_2-CH_2-SH = -NH_3^+, NH_2-CH_2-CH_2-SH = -NH_2, Zn^{2+}, and H_3O^+). As shown in **Fig. 5d-i and Fig. S22a**, the electrostatic potential (ESP) of Zn^{2+} at 4.3592 eV was significantly higher than that of -NH_3^+ at 0.237 eV, strongly indicating a weak affinity of -NH_3^+ for Zn^{2+} due to the great difference of the charge. Similarly, as shown in **Fig. 5d-ii and Fig. S22b**, the sites based on -NH_2 functional groups exhibited an uncharged state EPS, indicating it would not affect H_3O^+ with a positive ESP of 0.5 eV. Conversely, H_3O^+ and -NH_3^+ showed similar EPS values (**Fig. 5d-i and Fig. S22b**), implying it would have significant repulsion effects.

Therefore, the -NH_3^+ functional sites on the Zn surface can repel H_3O^+ and the -NH_2 groups as zincophilic sites can absorb Zn^{2+}, while the opposite effect (such as Zn^{2+} repelled by -NH_3^+ and H_3O^+ attracted by -NH_2) was not detected.

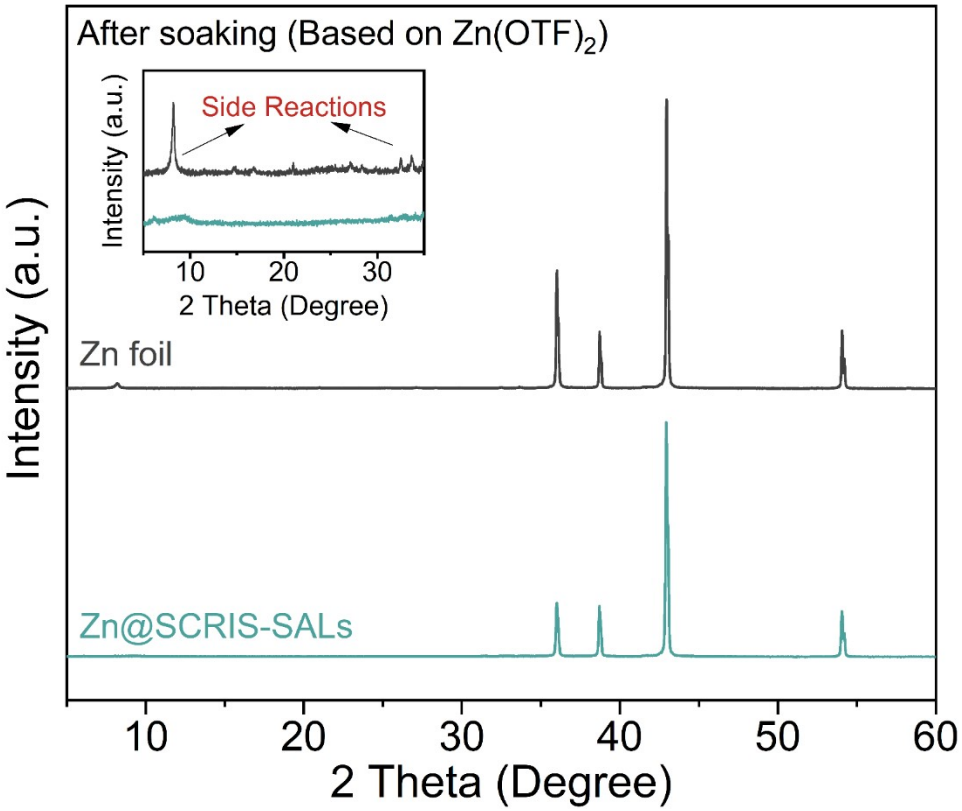

Fig. S23 XRD pattern of bare Zn after soaking in 2 M $Zn(OTF)_2$, bare Zn after soaking in 2 M $Zn(OTF)_2$ with 1 mM cysteamine (Zn@SCRIS-SALs) for 12 h, wherein the by-product of $Zn_x(OTF)_y(OH)_{2x-y}{\cdot}nH_2O$ after soaking is in the inset.[13]

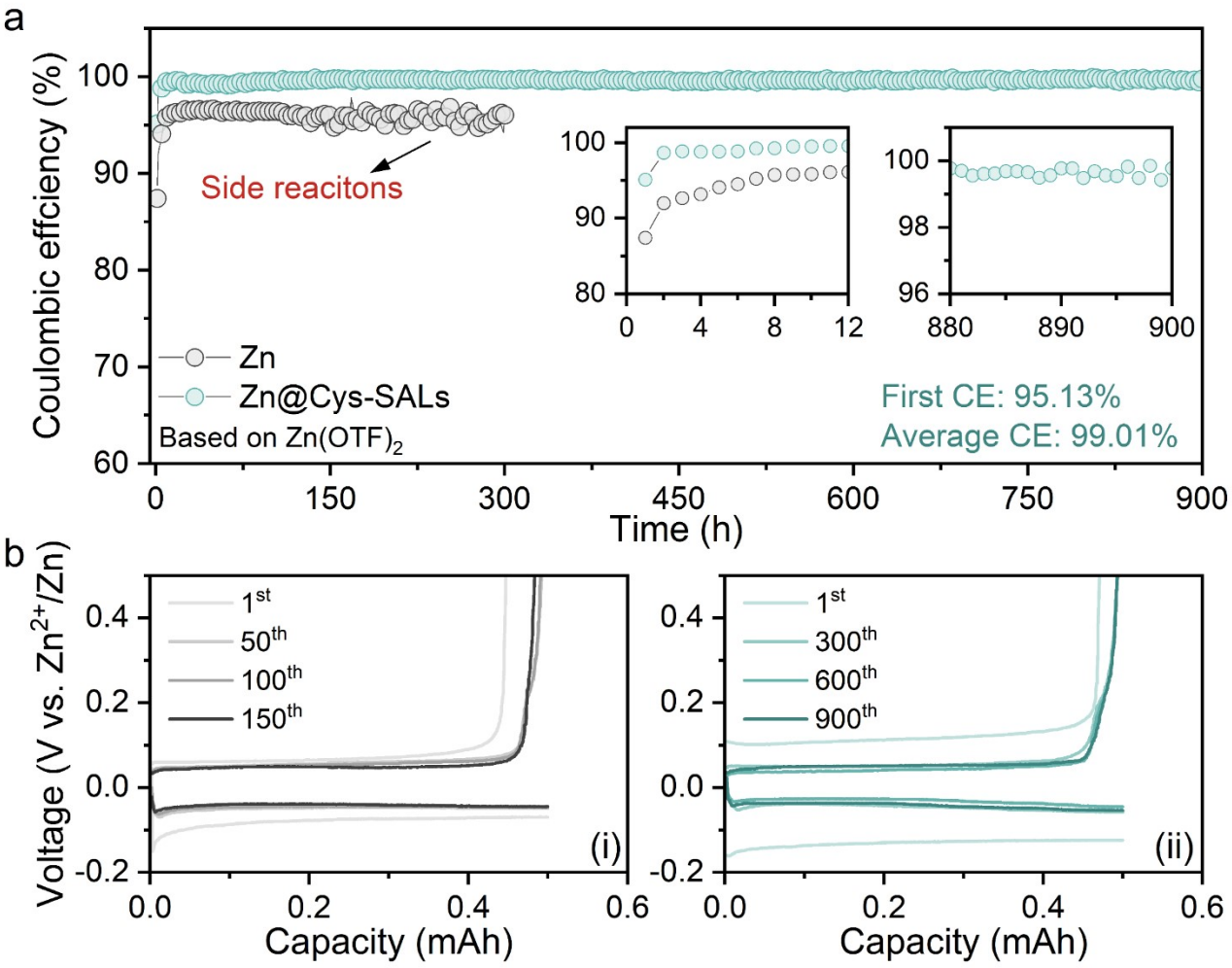

Fig. S24 CE evolution of the bare Zn and Zn@SCRIS-SALs foil on cycling Zn||Cu asymmetric cells under an areal capacity of 0.5 mA h cm^{-2} at 1 mA cm^{-2}, where the regions (0-12 h and 740 - 800 h) are in the inset. (b) Voltage profiles of selected cycles corresponding to the region (i)-bare Zn (the 1^{st}, 50^{th}, 100^{th}, and 150^{th} cycles) and region (ii)-Zn@SCRIS-SALs (1^{st}, 300^{th}, 600^{th}, and 900^{th} cycles).

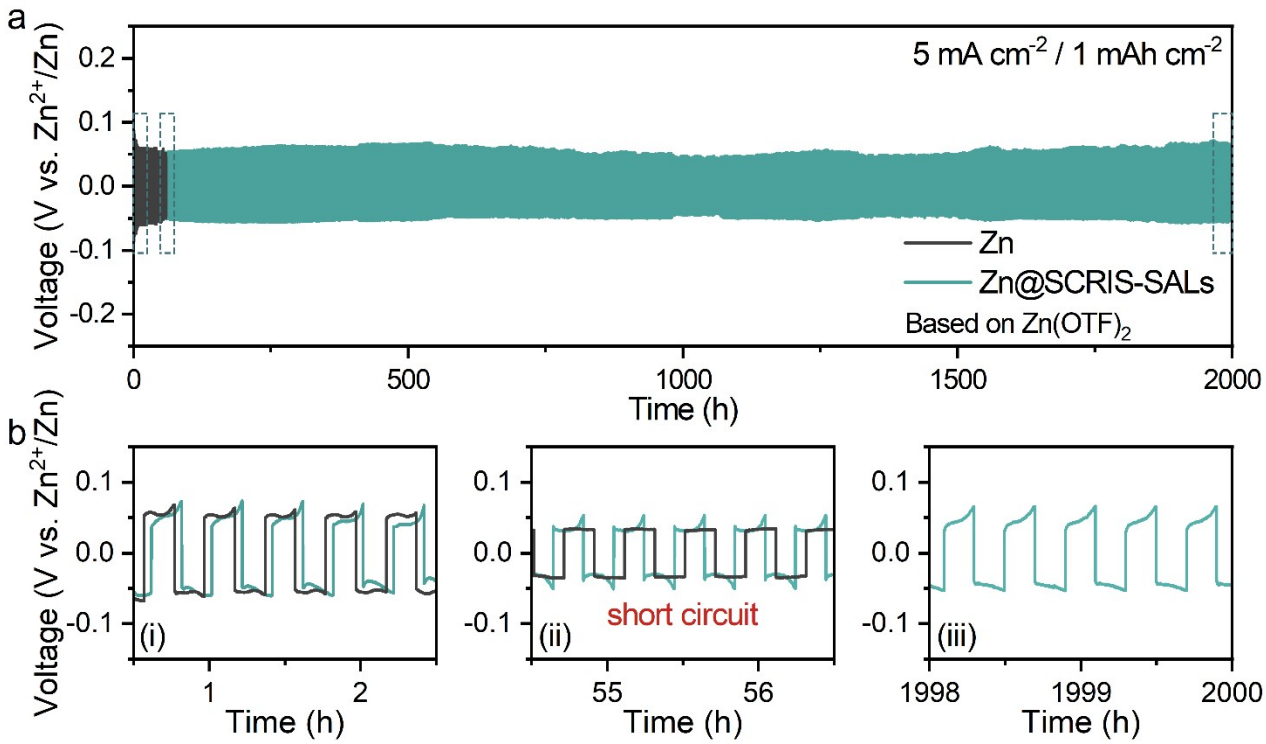

Fig. S25 Voltage-time curves of bare Zn and Zn@SCRIS-SALs symmetric cells on 2 M $Zn(OTF)_2$ without and with 1 mM cysteamine under a capacity of 1 mA h cm^{-2} at 5 mA cm^{-2} and (b) the selected cycles corresponding to the region (i) (0-2 h), region (ii) (55-56 h) and region (iii) (1998-2000 h) in cycling performances.

Note: As revealed in **Fig. S25**, based on 2 M $Zn(OTF)_2$ with 1 mM cysteamine electrolytes, Zn@SCRIS-SALs delivered a more stable plating/stripping cycling life for 200 hours at a high density of 5 mA cm^{-2} with an areal capacity of 1 mA h cm^{-2} compared to the inferior cycling performance of the bare Zn anode, which failed after 300 h (**Fig. S25b-ii**), consistent with the result of $ZnSO_4$ with cysteamine electrolytes. Therefore, Zn@SCRIS-SALs mediated by the partial protonation of functional groups can not only repulse $H^+ \cdot H_2O$ by the surface positively charge reinforced ($-NH_3^+$) state, but also offer more zinc-philic sites by the ion-selective ($-NH_2$) state, resulting in suppressing side reactions (HER) and Zn dendrites.

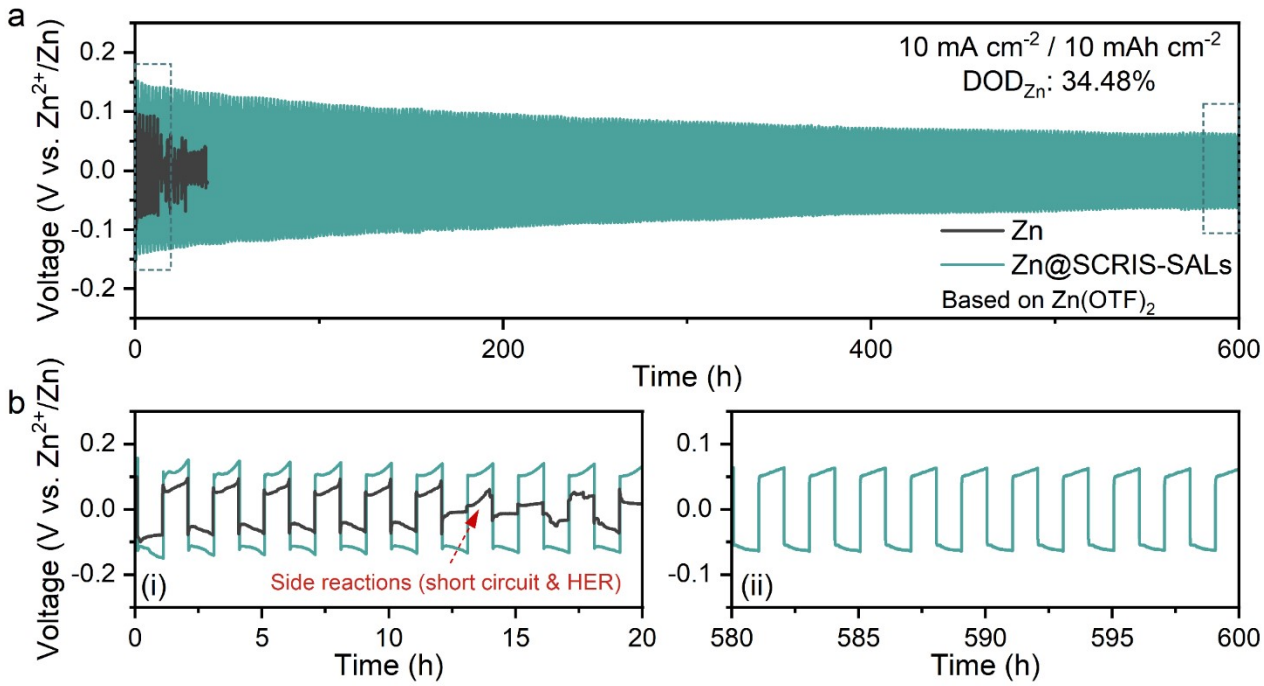

Fig. S26 Voltage-time curves of bare Zn and Zn@SCRIS-SALs symmetric cells on 2 M $Zn(OTF)_2$ without and with 1 mM cysteamine under a high areal capacity of 10 mA h cm^{-2} at a high current density of 10 mA cm^{-2} and (b) the selected cycles corresponding to the region (i) (0-20 h) and region (ii) (580-600 h) in cycling performances.

Note: as shown in **Fig. S26**, Zn@SCRIS-SALs symmetric cells also displayed a superior DOD_{Zn} (34.48%) cycling stability for 250 h under an areal high capacity of 20 mA h cm^{-2} at 20 mA cm^{-2} based on 2 M $Zn(OTF)_2$ with 1 mM cysteamine, whereas bare Zn symmetric cells failed in a short time (**Fig. S26b-i**) under the same test condition due to the severe working requirement-induced cell swelling by gas and short circuits by Zn dendrites.

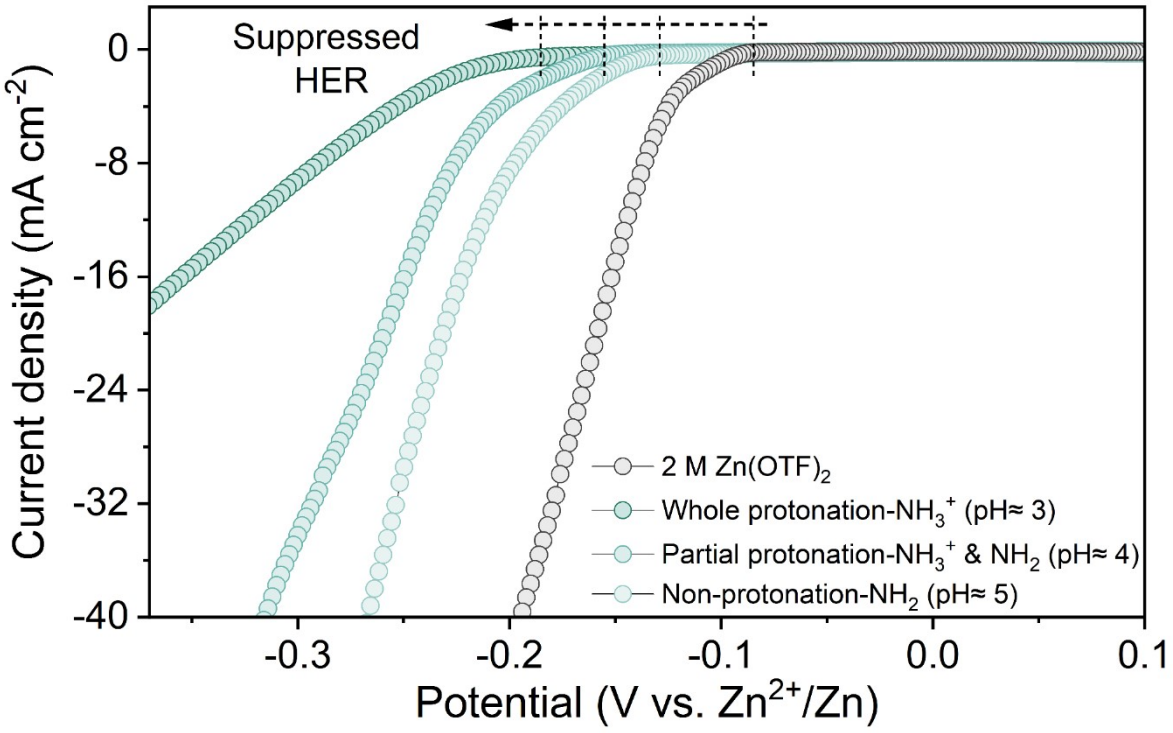

Fig. S27 LSV curves showing the suppression of water decomposition in 2 M $Zn(OTF)_2$ (bare Zn) and 2 M $Zn(OTF)_2$ with 1 mM cysteamine (Zn@SCRIS-SALs) under different pH conditions.

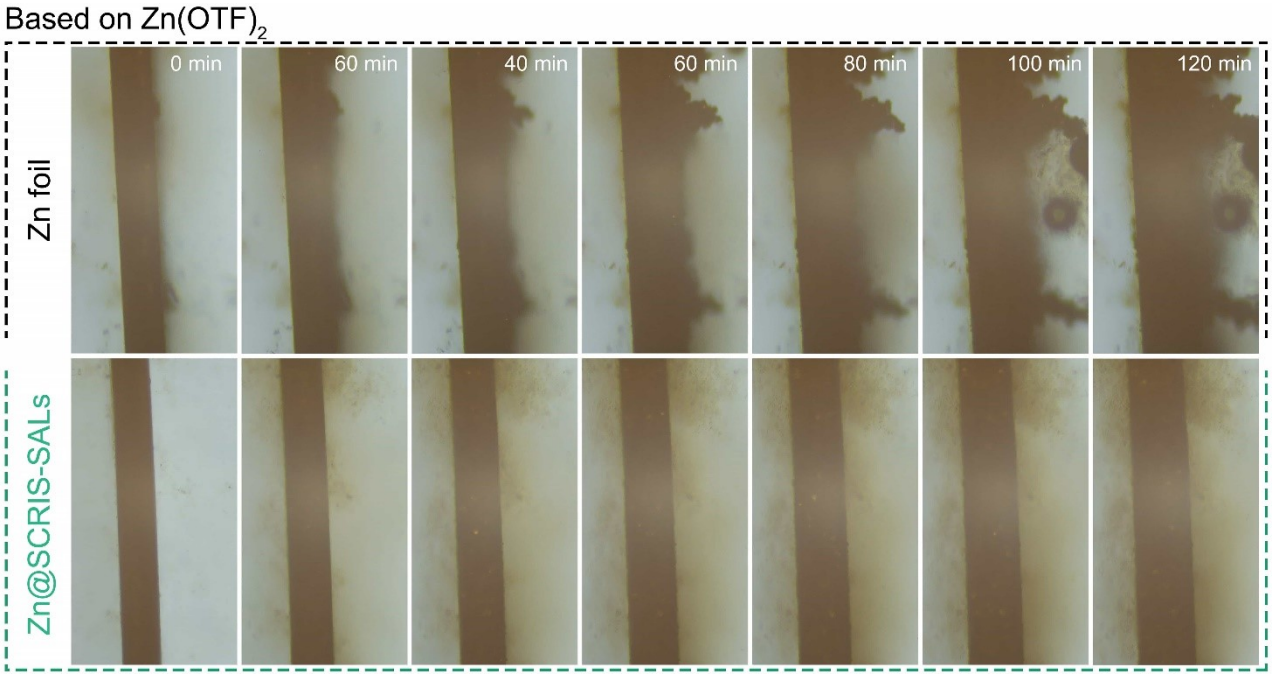

Fig. S28 Operando optical microscopy images in bare Zn (Top) and Zn@SCRIS-SALs (Bottom) symmetric transparent cells recorded after specified cycles in the deposited state.

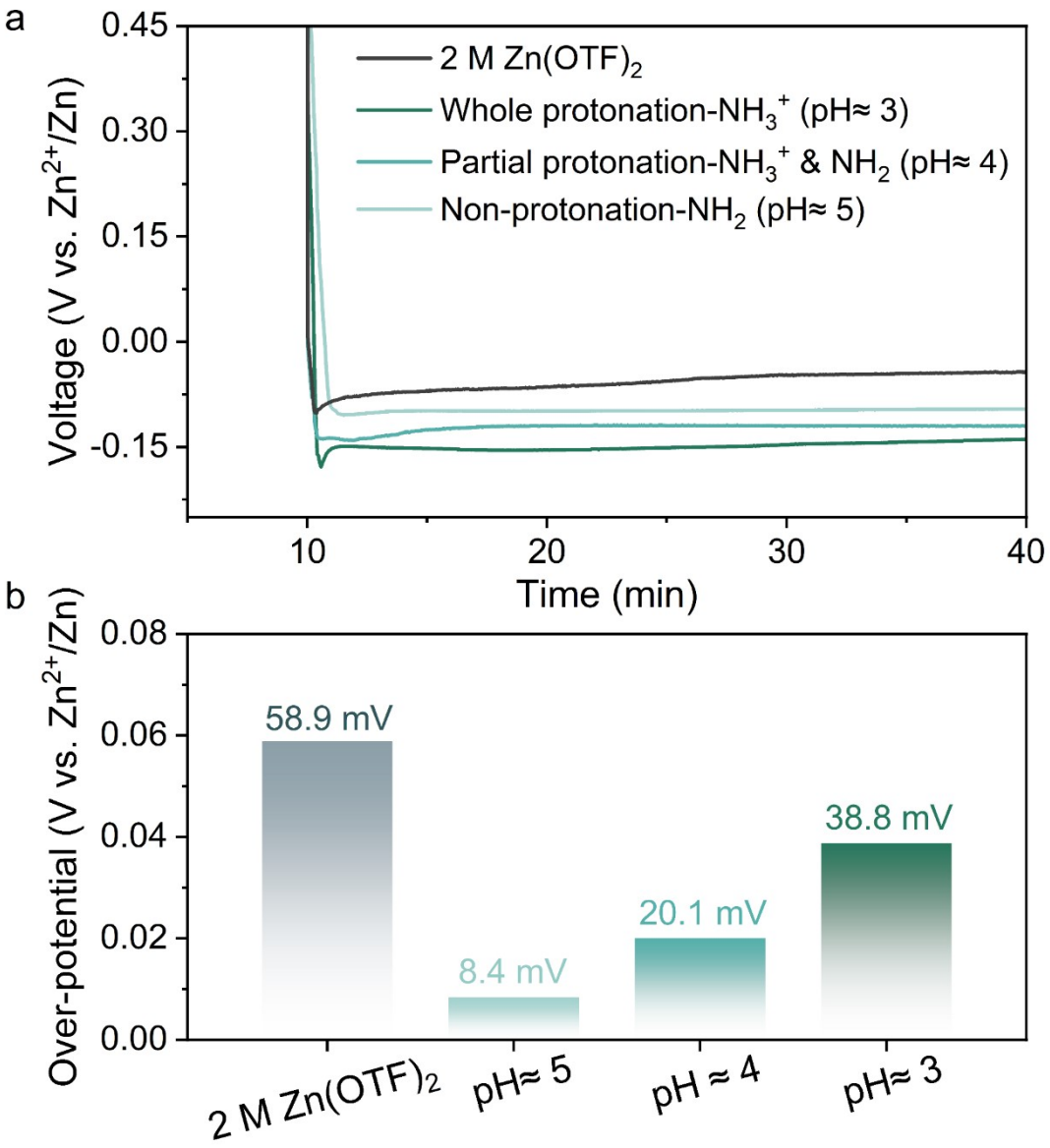

Fig. S29 The first plating voltage profiles of Zn||Cu cells at 5 mA cm^{-2} and 1 mAh cm^{-2} corresponding to (b) the overpotential of the initial nucleation process under different pH conditions.

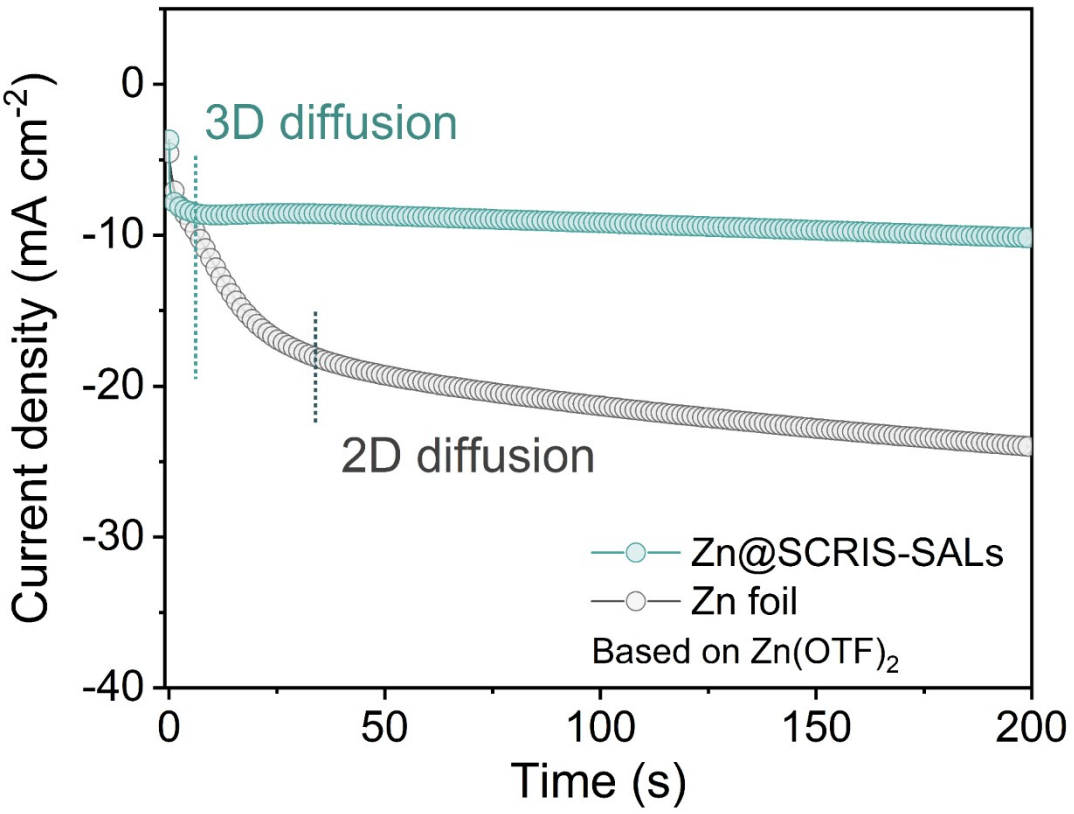

Fig. S30 Chronoamperograms (CA) of symmetric cells of bare Zn in 2 M $Zn(OTF)_2$ and Zn@SCRIS-SALs in 2 M $Zn(OTF)_2$ with 1 mM cysteamine at -150 mV overpotential.

Note: Schematics of the Zn^{2+} diffusion and reduction processes on bare Zn in 2 M $Zn(OTF)_2$ and Zn@SCRIS-SALs anodes in 2 M $Zn(OTF)_2$ with 1 mM cysteamine, showing that the Zn@SCRIS-SALs anode with 3D diffusion can be smooth in Zn deposition, consistent with the Zn@SCRIS-SALs based on $ZnSO_4$ electrolyte system.[11]

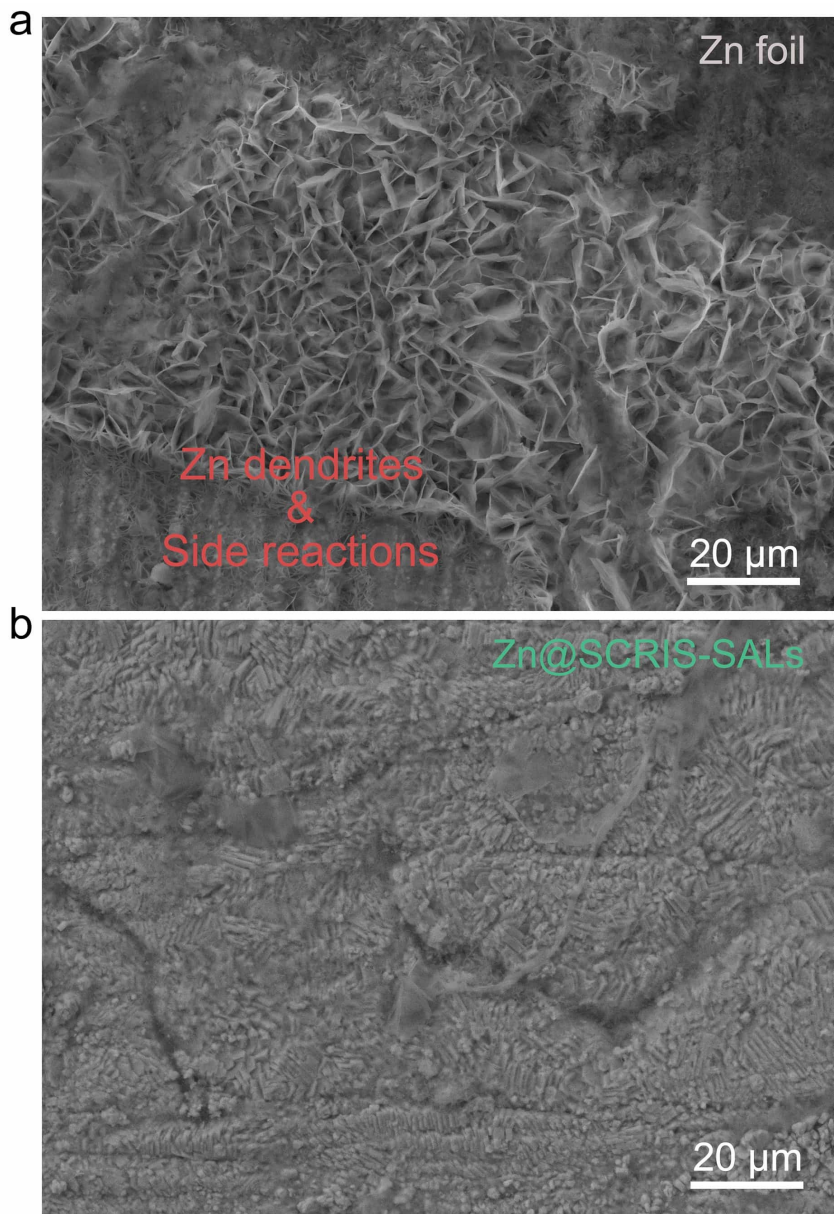

Fig. S31 SEM images of (a) bare Zn and (b) Zn@SCRIS-SALs anodes with partial protonation surface (pH≈ 4) in the deposited state at 5 mA cm^{-2} and 1 mAh cm^{-2} after 100 h cycles.

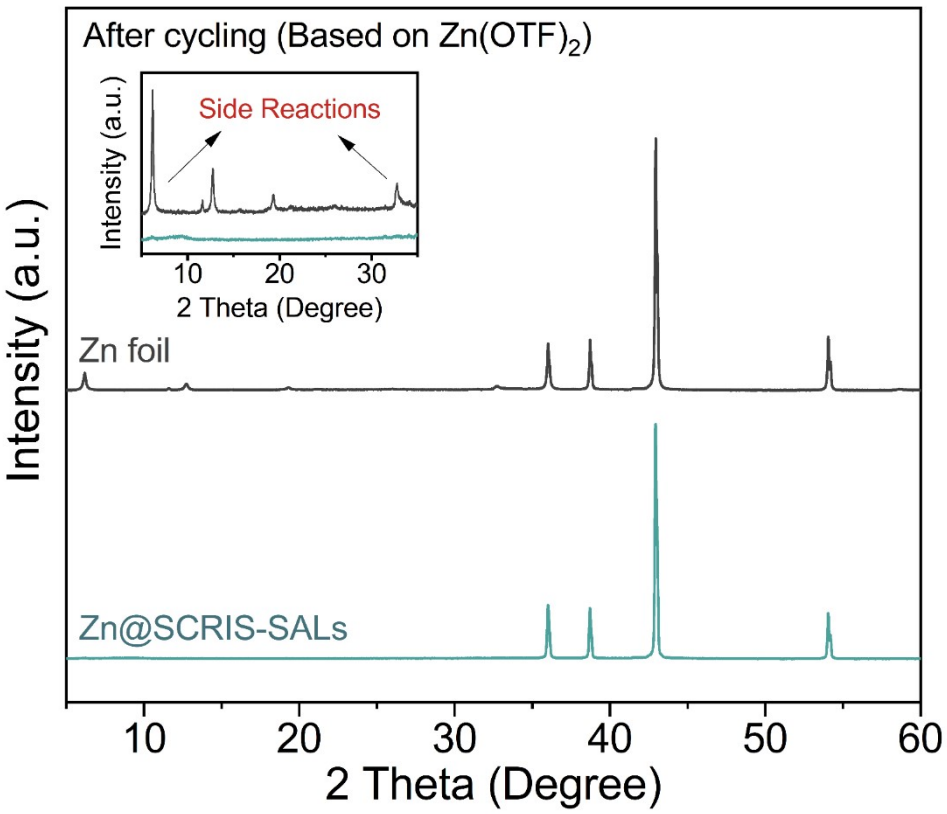

Fig. S32 XRD pattern of bare Zn in 2 M $Zn(OTF)_2$, Zn@SCRIS-SALs in 2 M $Zn(OTF)_2$ with 1 mM cysteamine anodes after 100 h cycles with a capacity of 1 mA h cm^{-2} at 5 mA cm^{-2}, wherein the by-product of $Zn_x(OTF)_y(OH)_{2x-y}{\cdot}nH_2O$ after 100 h cycles is in the inset.[13]

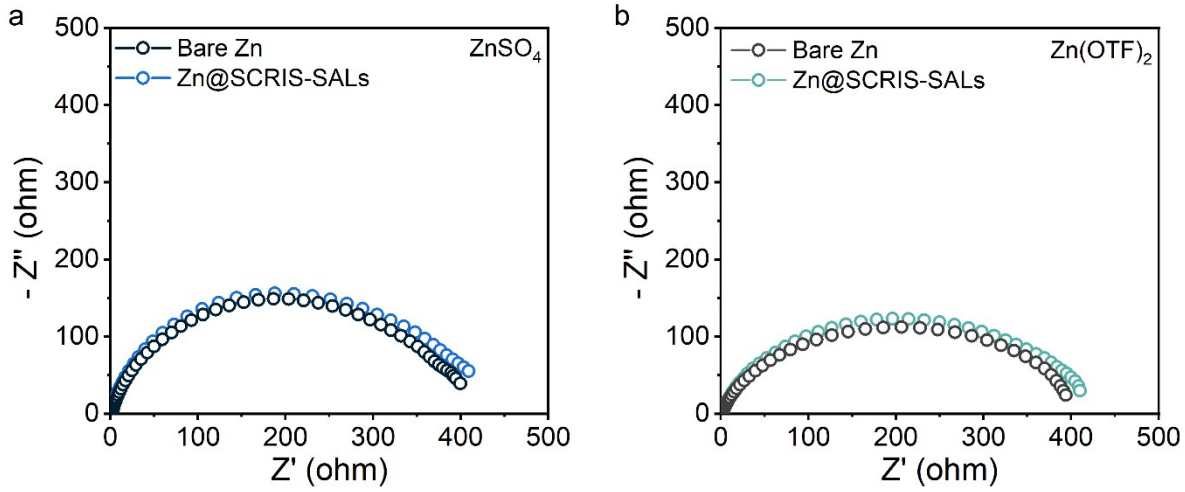

Fig. S33 EIS curves of Zn@SCRIS-SALs and bare Zn in symmetric cells under (a) $ZnSO_4$ and (b) $Zn(OTF)_2$ electrolyte systems.

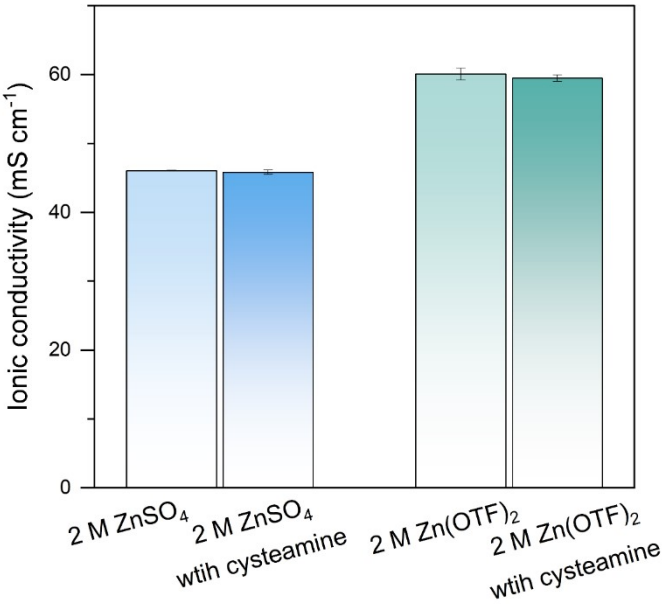

Fig. S34 The ionic conductivity of different electrolytes, wherein the data was collected by the ionic conductive meter (Brand: REX, Model: DDBJ-350).

Note: the ionic conductivity of a battery electrolyte plays a critical role in determining its charging rate, which allows ions to move more freely within the electrolyte, facilitating faster charge and discharge rates for the battery (Ref). As displayed in **Fig. S34**, compared to pristine 2 M $ZnSO_4$ (46.06 mS cm^{-1}) and $Zn(OTF)_2$ (60.10 mS cm^{-1}) electrolytes, the introduction of 1 mM cysteamine additives exhibited almost no effect on the ionic conductivity of the electrolyte (45.83 mS cm^{-1} in $ZnSO_4$ with cysteamine; 59.50 mS cm^{-1} in $Zn(OTF)_2$ with cysteamine), which can be attributed to the low amount and small-sized molecular structure of cysteamine additives. This feature could enable the electrolyte to keep favorable rate capabilities for battery operation.

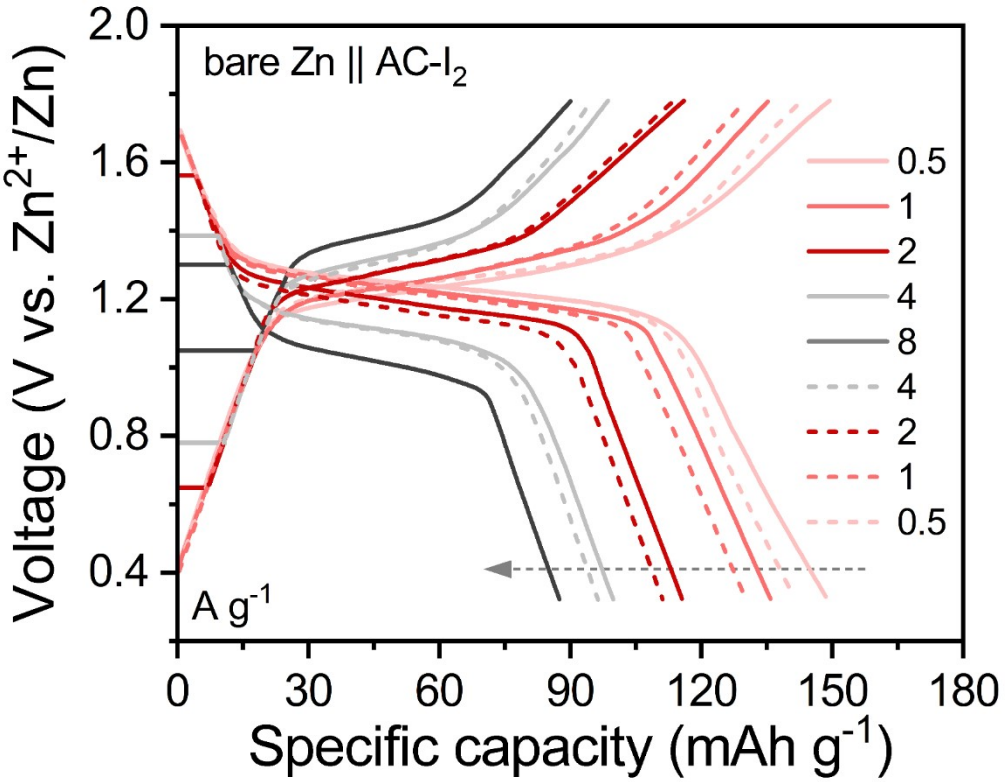

Fig. S35 Galvanostatic charge-discharge profiles of bare Zn || AC-I_2 coin cells with active materials loading of 3 mg cm^{-2} at different current densities (0.5, 1, 2, 4, and 8 A g^{-1}).

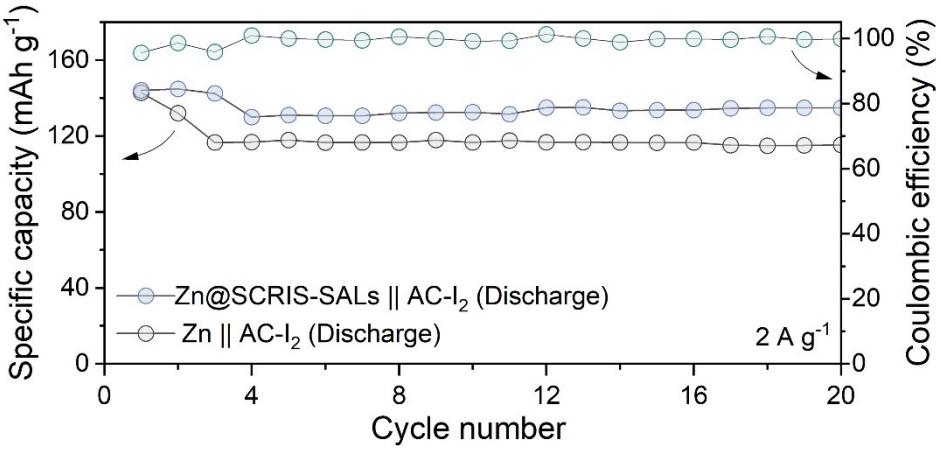

Fig. S36 Cycling performance of Zn@SCRIS-SALs || AC-I_2 and bare Zn || AC-I_2 batteries for the first 20 cycles at the current density of 2 A g^{-1}.

Note: As shown in **Fig. S36**, we extracted details of the cycling performance for the first 20 cycles. From the initial process results, it can be observed that electrolyte additives have no effect on the full battery capacity. However, as cycling progresses, the capacity decreased due to thermodynamic and kinetic issues inherent in the bare Zn electrode during the initial stages. Regarding polarization issues, the high reversibility of Zn@SCRIS-SAL could prevent the passivation of the Zn metal surface, resulting in lower polarization of the full battery.

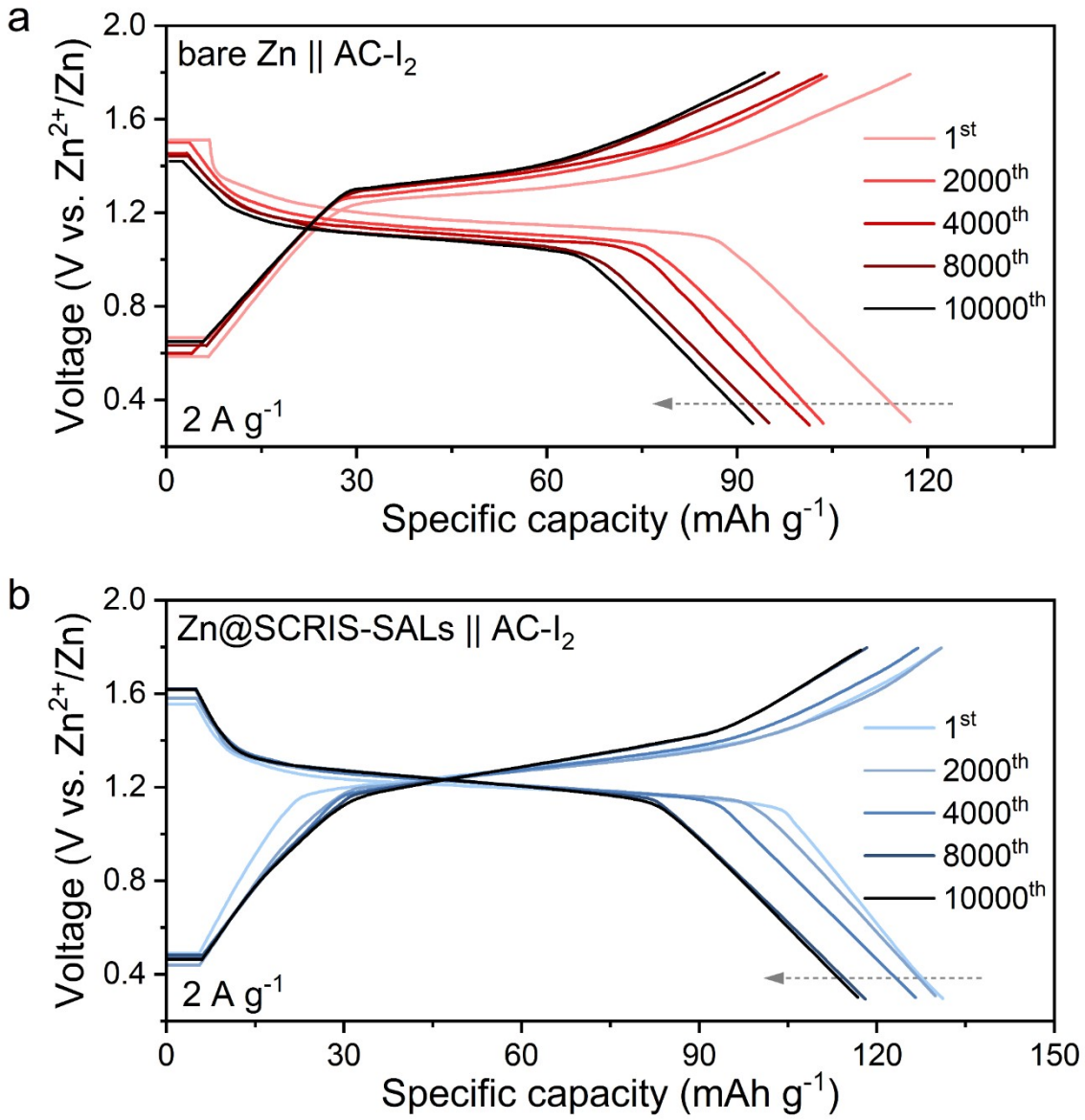

Fig. S37 Galvanostatic charge-discharge profiles of (a) bare Zn || AC-I_2 and (b) Zn@SCRIS-SALs || AC-I_2 coin cells with active materials loading of 3 mg cm^{-2} at 2 A g^{-1}.

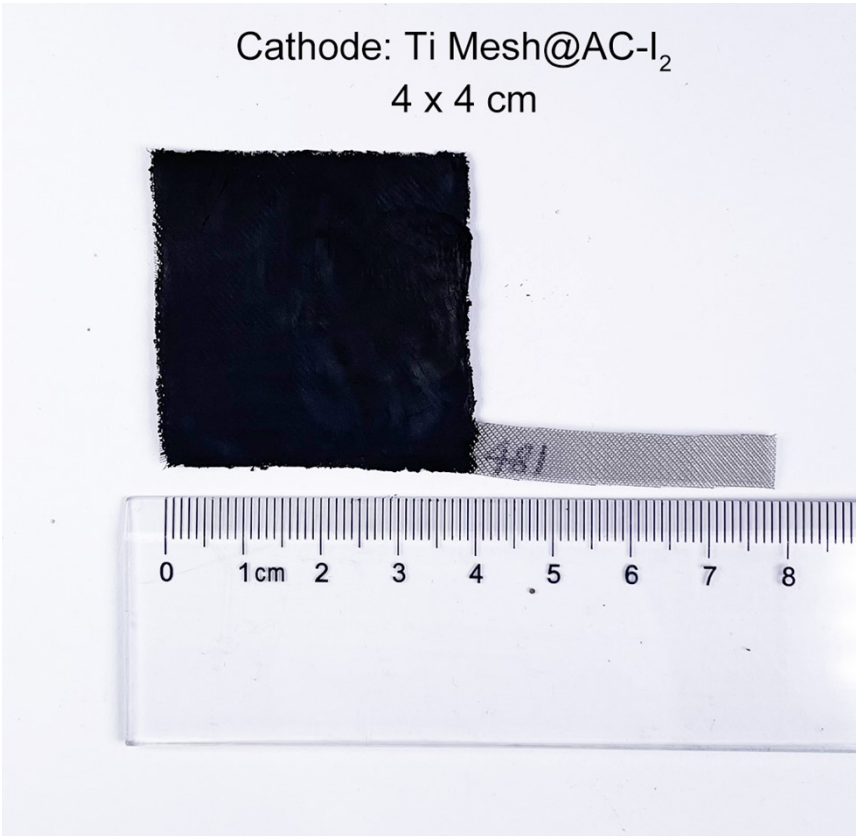

Fig. S38 Photographs & size of AC-I_2 cathodes for pouch cells.

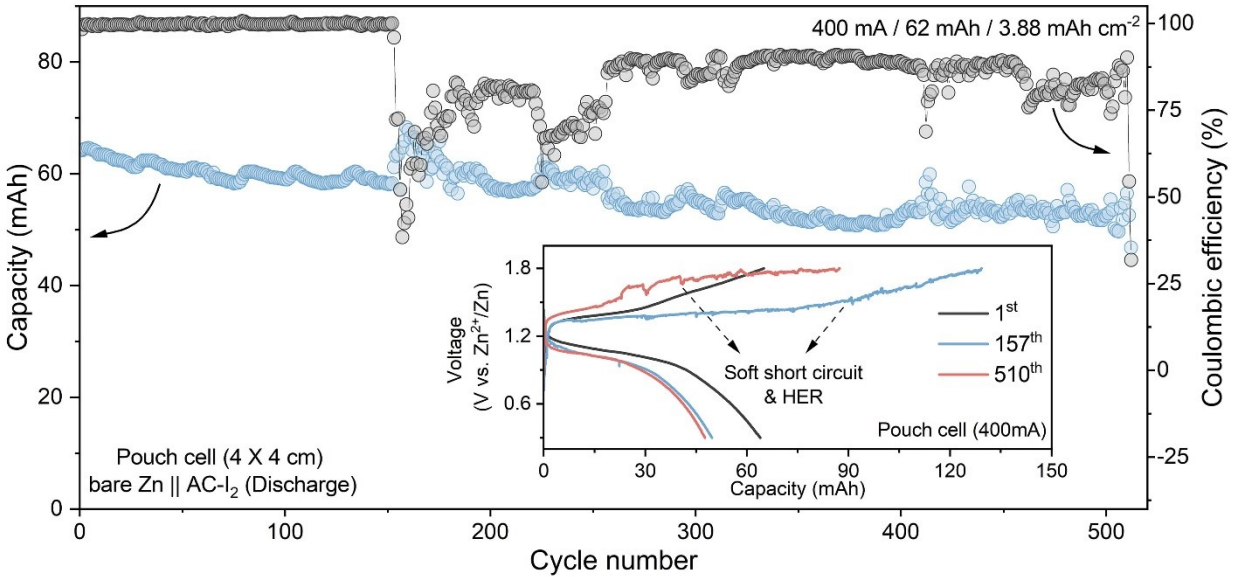

Fig. S39 Cycling performance of bare Zn || AC-I_2 battery in pouch cells with an areal capacity of 3.88 mAh cm^{-2} under harsh test conditions (400 mA), wherein photographs and voltage profiles of Zn@SCRIS-SALs pouch batteries at 1st, 157^{th,} and 510th cycles are in the inset.

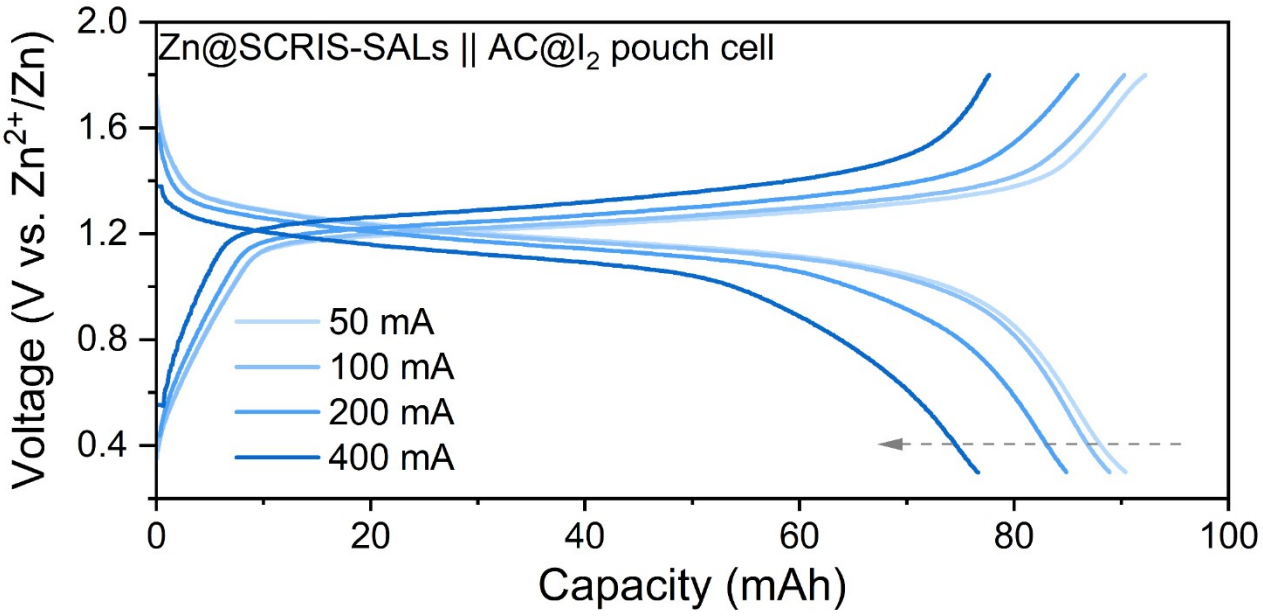

Fig. S40 Galvanostatic charge-discharge profiles of Zn@SCRIS-SALs || AC-I_2 pouch cells with active materials loading of 30.5 mg cm^{-2} at different current densities (50, 100, 200, and 400 mA).

Table S1 Chemical bond species vs. B.E. for SCRIS-SALs.

Element	*Zn@SCRIS-SAL after depth etching for 10s (eV)*	*Chemical Bond Specie*
C 1s A	284.8	C-C/C-H
C 1s B	285.75	C-S & C-N
N 1s A	399.1	$-NH_2$
N 1s B	399.65	$-NH_3^+$
S 2p A	162.11 & 163.61	S-Zn (thiol)
S 2p B	168.22 & 169.91	$-SO_x^{2-}$
Zn $2p_{3/2}$ & $2p_{1/2}$	1021.25 & 1043.95	Zn-S (thiol) & Zn^{2+}
Zn $2p_{3/2}$ & $2p_{1/2}$	1022.5 & 1045.75	Metallic Zn^0

Table S2 Comparison of aqueous Zn battery performance for this work with reported protective coatings and electrolyte additives.

Number	***Materials***	***Electrolytes***	***Current density (mA cm^{-2})***	***Cycling life (h)***	***Areal capacity per cycle (mAh cm^{-2})***	***Cumulative capacity (Ah cm^{-2})***	***Depth of $discharge_{Zn}$ (DOD %)***	***Reference***
1	TiO_2 coating	$ZnSO_4$	2	280	2	0.28	12.2	*Nat Commun,*, **2022**, *11*, 3961.
2	Mxene coating	$ZnSO_4$	0.2	800	0.2	0.25	3.41	*Angew. Chem.*, **2021**, *133*, 2897
3	ZnF_2 coating	$ZnSO_4$	5	1000	/	/	/	*Adv.Mater.*, **2021**, *33*, 2007388
4	Zn (002)	$ZnSO_4$	1	500	1	1.113	0.25	*Adv. Mater.*, 2021, *33*, 2100187
5	GFA-Zn coating	$ZnSO_4$	1	2000	3	0.1	1.05	*Energy Environ. Sci.*, **2022**, *15*, 1086
6	DES-Zn	$ZnSO_4$	1	1050	3	0.6	40	*Energy Environ. Sci.*, **2022**, *15*, 2889
7	Zn	$ZnSO_4$ with Cyclodextrin	10	160	1	0.5	30	*J. Am. Chem. Soc.*, **2022**, *144*, 11129
This work	Zn@SCRIS-SALs	$ZnSO_4$ or $Zn(OTF)_2$ with cysteamine	10	2500	1	2.7	68.96	This work

References

1 Q. Zhao, W. Huang, Z. Luo, L. Liu, Y. Lu, Y. Li, L. Li, J. Hu, H. Ma and J. Chen, *Sci. Adv.*, 2018, **4**, eaao1761.

2 W. Kohn and L. J. Sham, *Physical review*, 1965, **140**, A1133.

3 A. V. Marenich, C. J. Cramer and D. G. Truhlar, *The Journal of Physical Chemistry B*, 2009, **113**, 6378-6396.

4 S. Grimme, *Journal of computational chemistry*, 2006, **27**, 1787-1799.

5 D. V. Vezenov, A. Noy, L. F. Rozsnyai and C. M. Lieber, *J. Am. Chem. Soc.*, 1997, **119**, 2006-2015.

6 X. Song, Y. Ma, C. Wang, P. M. Dietrich, W. E. S. Unger and Y. Luo, *J. Phys. Chem. C*, 2012, **116**, 12649-12654.

7 A. Cossaro, M. Dell'Angela, A. Verdini, M. Puppin, G. Kladnik, M. Coreno, M. de Simone, A. Kivimäki, D. Cvetko, M. Canepa and L. Floreano, *J. Phys. Chem. C*, 2010, **114**, 15011-15014.

8 H. Chen, C. Dai, F. Xiao, Q. Yang, S. Cai, M. Xu, H. J. Fan and S. J. Bao, *Adv. Mater.*, 2022, **34**, 2109092.

9 D. Ledwith, S. C. Pillai, G. W. Watson and J. M. Kelly, *Chem. Commun.*, 2004, 2294-2295.

10 S. J. Zhang, J. Hao, D. Luo, P. F. Zhang, B. Zhang, K. Davey, Z. Lin and S. Z. Qiao, *Adv. Energy Mater.*, 2021, **11**, 2102010.

11 Z. Zhao, J. Zhao, Z. Hu, J. Li, J. Li, Y. Zhang, C. Wang and G. Cui, *Energy Environ. Sci.*, 2019, **12**, 1938-1949.

12 M. Yan, N. Dong, X. Zhao, Y. Sun and H. Pan, *ACS Energy Lett.*, 2021, **6**, 3236-3243.

13 Y. Dong, L. Miao, G. Ma, S. Di, Y. Wang, L. Wang, J. Xu and N. Zhang, *Chem. Sci.*, 2021, **12**, 5843-5852.